Journal of Translational Medicine

RESEARCH

Open Access

Near infrared photo-bacterialflora modulation technology realized controlling periodontitis: modulation of disease-associated dysbiosis in oral microbiota using near infrared photo-antibacterial targeting therapy (NIR-PAT^2)

Hiroshi Maruyama[1,5], Kazuhide Sato[2,3,4,7*], Kiyoshi Sakai[1,7*], Hirotoshi Yasui[2], Ryu Okada[2], Li Xinheng[5], Koji Umeda[6], Shofiqur Rahman[6], Van Sa Nguyen[6] and Hideharu Hibi[1,5]

Abstract

Background Periodontitis is a complex polymicrobial disease driven by synergistic interactions within a dysbiotic oral community. Within this network, *Porphyromonas gingivalis* acts as a keystone pathogen that orchestrates the pathogenic transformation of the microbiota. Current broad-spectrum antimicrobials often disrupt the entire microbial ecosystem and release immunogenic lipopolysaccharides (LPS). We aimed to develop a targeted approach, Near-Infrared Photo-Antibacterial Targeting Therapy (NIR-PAT^2), using an antibody-photosensitizer conjugate (IgY-IR700) to reduce *P. gingivalis* load within this polymicrobial complex and modulate the community profile.

Methods We evaluated the binding and bactericidal mechanism of NIR-PAT^2 in vitro compared to antimicrobial photodynamic therapy (aPDT), using scanning electron microscopy (SEM) and endotoxin assays. In vivo, a ligature-induced periodontitis mouse model was used to assess therapeutic effects on alveolar bone resorption and microbiome community structure (16 S rRNA sequencing).

Results In vitro, NIR-PAT^2 eliminated *P. gingivalis* without affecting human cells. SEM analysis revealed a distinct mechanism: unlike aPDT, which caused bacterial disintegration, NIR-PAT^2 induced lethal transmembrane perforations while maintaining structural integrity. In parallel, endotoxin assays demonstrated that NIR-PAT^2 treatment significantly suppressed LPS release compared to aPDT. In vivo, NIR-PAT^2 treatment significantly inhibited alveolar bone resorption. Crucially, microbiome analysis demonstrated that NIR-PAT^2 did not merely eliminate the environment but induced a compositional shift toward a health-associated profile. By suppressing *Porphyromonas*, the treatment facilitated the partial restoration of commensal genera such as *Streptococcus*, disrupting the dysbiotic network.

*Correspondence:
Kazuhide Sato
sato.kazuhide.k5@f.mail.nagoya-u.ac.jp
Kiyoshi Sakai
sakai.kiyoshi.j0@f.mail.nagoya-u.ac.jp

Full list of author information is available at the end of the article

Conclusions This study suggests that NIR-PAT^2 functions as a "Near-Infrared Photo-Bacterialflora Modulation (NIR-PBAM)" technology. By targeting a keystone pathogen within the polymicrobial community, NIR-PBAM offers a strategy to partially restore microbial balance while presenting a potential advantage in limiting LPS release, thus overcoming the ecological disruption caused by conventional broad-spectrum antimicrobials.

Keywords *Porphyromonas gingivalis*, Periodontitis, IR700Dx, Near infrared photoimmunotherapy, NIR-PAT^2, Photo-antimicrobial therapies, IgY, Near infrared photo-bacterialflora modulation (NIR-PBM) technology

Graphical Abstract

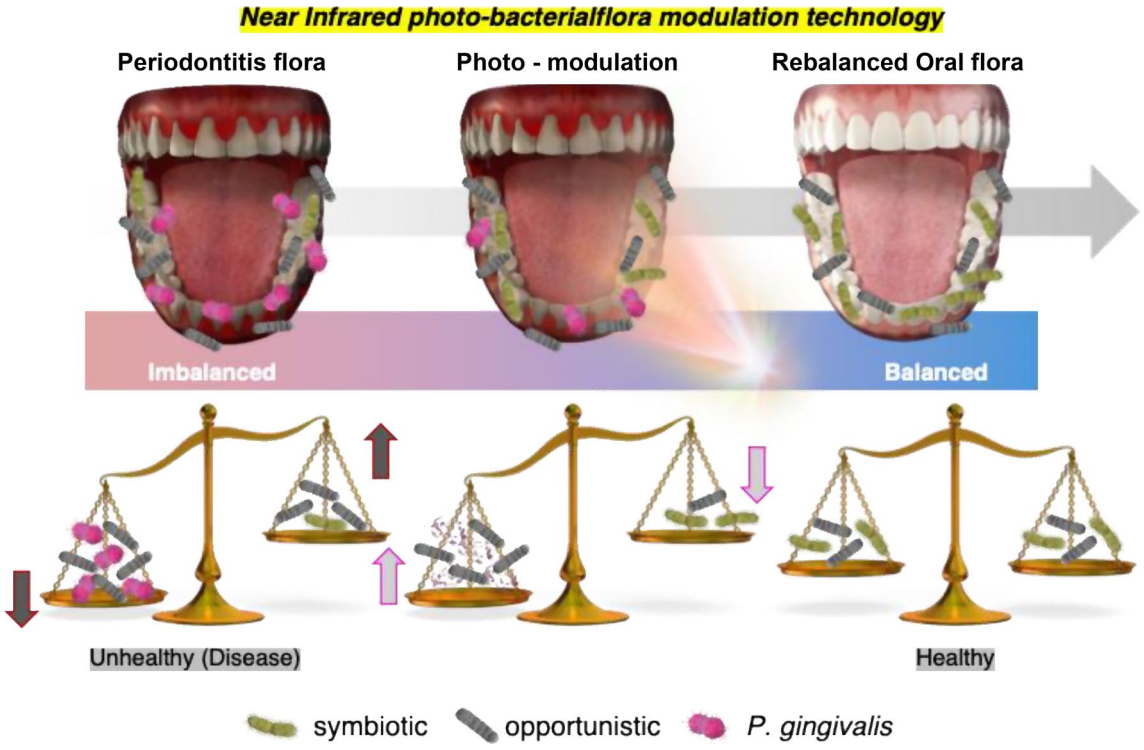

Introduction

In recent years, numerous associations between various diseases and abnormal oral and gut microbiota have been reported, including multiple sclerosis, rheumatoid arthritis, asthma, non-alcoholic fatty liver disease, obesity, and periodontitis [1]. Oral and gut microbiota exert multiple effects on host immunity, and disturbances in the gut microbiota may directly impact immune-mediated diseases [1]. The causes of dysbiosis include loss of symbionts, loss of diversity, and a rapid increase in pathogenic symbionts. The loss of symbionts is partially caused by a decrease or complete loss of commensal bacteria in the bacterial flora, resulting from non-selective disinfection with antimicrobial agents [2]. The loss of diversity may be influenced by dietary patterns [3]. A rapid increase in pathogenic symbionts occurs due to a disruption of the bacterial flora balance by commensal microflora members, which can cause disease [4, 5]. The first-line treatment for infections and inflammation caused by an increase in pathogenic symbionts is the use of antimicrobials; however, the use of antimicrobials can lead to further loss of symbionts [1]. Therefore, restoring abnormal bacterial flora to a normal state could be an ideal treatment strategy.

Traditionally, periodontitis was viewed as a simple infection; however, it is now recognized as a complex polymicrobial disease driven by synergistic interactions within the oral microbiota and a subsequent aberrant host immune response. Periodontitis is typically initiated by a shift from symbiotic to dysbiotic microbial communities. In this process, 'keystone pathogens' such as *Porphyromonas gingivalis*, even at low abundance, can remodel the surrounding commensal bacteria into a highly inflammatory state [6]. This microbial dysbiosis triggers an aberrant host immune response, leading to chronic inflammation and subsequent destruction of the periodontal ligament and alveolar bone. As a result, quality of life, including tooth loss and difficulties in mastication and oral function. In addition, the systemic inflammatory burden linked to periodontitis has been

associated with various non-communicable diseases, such as diabetes, cardiovascular disease, and rheumatoid arthritis [7–12], significantly impacting healthy life expectancy.

Periodontitis is primarily treated using mechanical debridement, such as tooth brushing, scaling, root planing, and professional mechanical tooth cleaning [13]. In severe periodontitis, the morphology of periodontal tissue is complicated by alveolar bone destruction, making mechanical debridement challenging. In these cases, adjuvant therapy with antimicrobial agents is required [13]. Antimicrobial resistance is a global problem [14, 15], and a previous study reported that 74.4% of patients with periodontitis harbor antimicrobial-resistant subgingival pathogens [16]. To overcome the antimicrobial-resistance, alternative therapy such as light therapy had been tried. Antimicrobial photodynamic therapy (aPDT) is used to overcome the limitations of conventional periodontal therapies [17–19]. It combines dyes and light irradiation to kill microorganisms by producing reactive oxygen species (ROS) [20]. The emergence of antibiotic-resistant bacteria has attracted renewed attention due to the antibacterial effects of aPDT. However, aPDT-induced ROS do not selectively target microbial cells and can be toxic to host tissues, moreover, even destroyed oral microflora. Visible light, particularly low-wavelength light, is toxic to healthy cells and does not penetrate deeply into tissues [20]. In addition, aPDT did not achieve significant success as an adjunctive therapy in the clinical stages of periodontitis [13, 21] .

Recently, a new cancer-targeted therapy called near-infrared photoimmunotherapy (NIR-PIT), which combines antibody–dye conjugates and near-infrared light, has emerged [22–25]. NIR-PIT uses a photosensitized silica phthalocyanine dye IRDye700Dx (IR700). The mAb-IR700 conjugate is able to target specific surface proteins overexpressed on cancer cell membranes, and a variety of tumor-cell surface targeting mAbs have been evaluated preclinically [23–29]. In 2020, cetuximab-IR700, an IR700-conjugated anti-EGFR monoclonal antibody (mAb), was conditionally approved for recurrent head and neck cancers by the Pharmaceuticals and Medical Devices Agency (PMDA) in Japan. The cell death mechanism of NIR-PIT is unique. Specifically, when the conjugate is irradiated with near-infrared light in the presence of sufficient electron donors, the hydrophilic side chain (silanol) of the IR700 molecule dissociates through a photochemical ligand reaction, and the remaining structure, including the antibody, rapidly becomes hydrophobic and aggregates. At the same time, the antibodies bound to the surface antigens also aggregate on the tumor cell membrane. The aggregation reaction of IR700 causes physical stress on the antigen-antibody complex and selectively destroys the target cells [30].

We recently developed NIR photoantimicrobial-targeted therapy (NIR-PAT^2) to treat infectious diseases. This therapy exerts antimicrobial effects against *Candida albicans*, by puncturing and deforming the fungus [31]. For NIR-PAT^2, as targeting molecules, we exploit IgY, which can be extracted from the egg yolk of chicken immunized with inactivated bacteria substrates and purified with using the Thiophilic Adsorption column. Since pathogens multiply faster than cancer cells, large quantities of antibodies are required for their treatment, making it difficult to achieve from a medical economic perspective. Therefore, we devised a method that utilizes IgY, which can be produced in large quantities at low cost. NIR-PAT^2 with IgY could be used for body surface and lumens, such as skin, hair, eye, digestive tract.

The optimal treatment for periodontitis should aim to restore periodontal tissue stability and a near-healthy oral bacterial community [32]. However, clinically usable treatment methods that aid in modulation oral dysbiosis have not yet been developed. Therefore, new technological development for controlling microbiota is highly desirable. The aim of this study was to develop a bacteria-targeted therapeutic modality using NIR-PAT^2. While we acknowledge the inherent limitations of single-pathogen targeting in a complex polymicrobial disease, we hypothesized that selectively eliminating a keystone species would disrupt the synergistic drivers of dysbiosis. We define this approach as a precision-modulating therapy, designed to selectively ablate *P. gingivalis* while preserving the ecological integrity of the oral community. Here, we demonstrate that NIR-PAT^2 successfully modulates oral dysbiosis, leading to the resolution of periodontitis and the restoration of a healthy-associated microbial profile in a murine model.

Materials and methods

Ethical statement

All in vivo animal experiments were conducted in compliance with the guidelines of the Guide for the Care and Use of Laboratory Animal Resources of the Nagoya University Animal Care and Use Committee (approval numbers: 2018–30096, 2019–31234, 2020–20104, 2021;M210695-001/ M210770, 2022; M220370-003/ M220372-003, 2023: M230269-002/ M230270-002, 2024: M240296-005/ M240295-002; 2025: M250149-003/ M250150-002). Mice were kept in compliance with the Act on Welfare and Management of Animals, Standards Relating to the Care and Keeping and Reducing Pain of Laboratory Animals, and Fundamental Guidelines for Proper Conduct of Animal Experiments and Related Activities in Academic Research Institutions. This study was performed in accordance with the ARRIVE 2.0 guidelines for animal research. All experiments about recombinant DNA were approved by the Nagoya

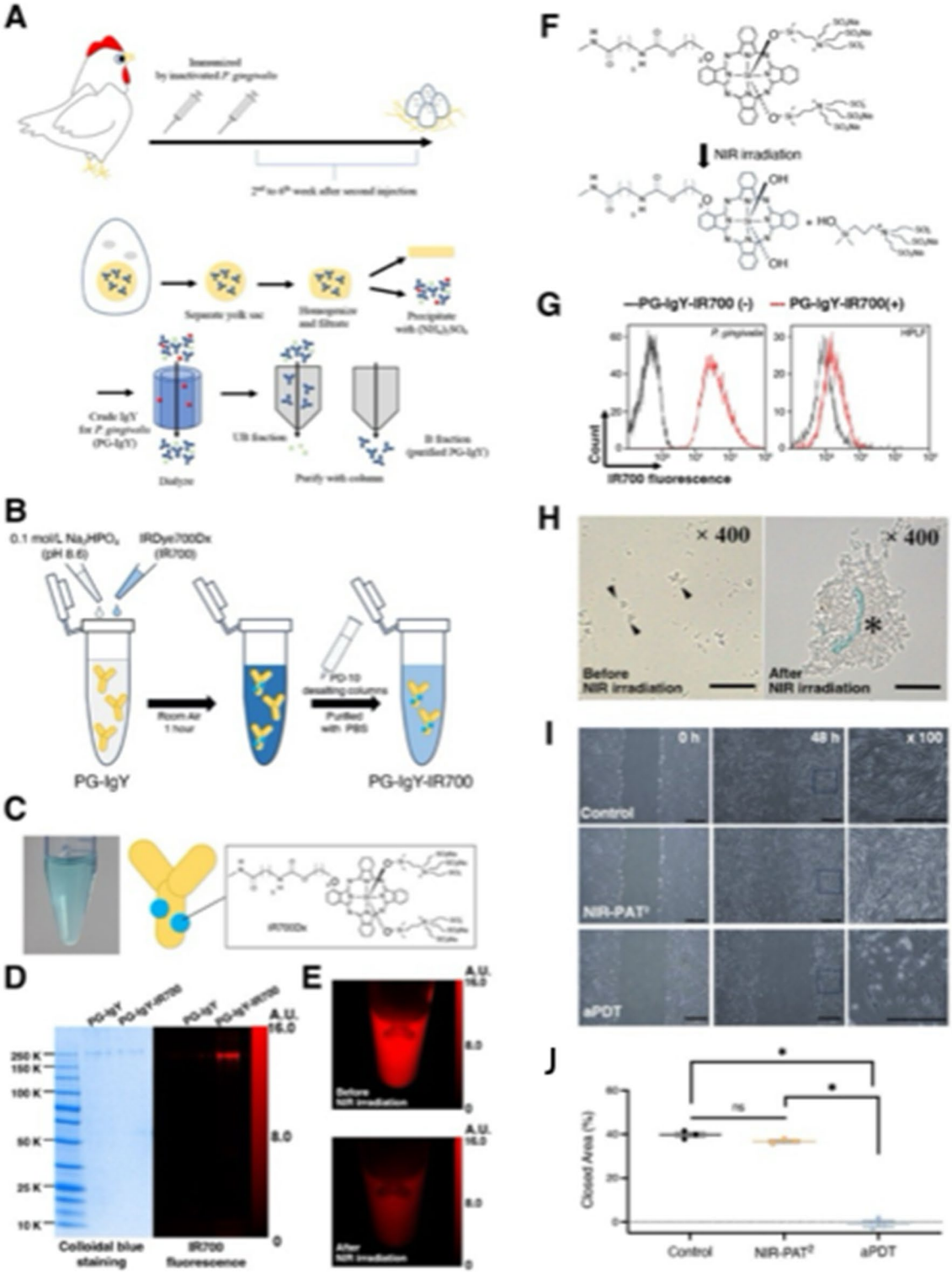

Fig. 1 (See legend on next page.)

University Recombinant DNA Experiment Safety Committee (approval number:16–138, 22–39).

Reagents

The water-soluble silica-phthalocyanine derivative IRDye 700DX NHS (IR700) ester was purchased from LI-COR

(See figure on previous page.)

Fig. 1 Preparation and evaluation of PG-IgY-IR700 against *P. gingivalis*.**(A)** Schematic illustration of the production of anti-*P. gingivalis* IgY (PG-IgY). Hens were immunized with inactivated *P. gingivalis*, and IgY was extracted and purified from the yolk sacs. **(B)** Schematic representation of the conjugation of IRDye700DX (IR700) to PG-IgY and the purification process using a PD-10 desalting column. **(C)** Photograph of the purified PG-IgY-IR700 solution appearing light blue (left) and the chemical structure of the IR700-conjugated antibody (right). **(D)** SDS-PAGE analysis of PG-IgY and PG-IgY-IR700. The gel was visualized using colloidal blue staining (left) and IR700 fluorescence imaging (right). Both proteins were detected at approximately 190 kDa, with fluorescence observed only in the conjugated form. **(E)** Fluorescence images of the PG-IgY-IR700 solution at 700 nm before and after near-infrared (NIR) irradiation (256 J/cm^2). The loss of fluorescence indicates the photochemical reaction. **(F)** Proposed mechanism of the photochemical reaction of the IR700 dye upon NIR irradiation, leading to ligand release and subsequent aggregation. **(G)** Flow cytometric analysis evaluating the binding specificity. PG-IgY-IR700 was incubated with *P. gingivalis* (left) or human periodontal ligament fibroblasts (HPLF) (right). A fluorescence shift was observed only for *P. gingivalis*. **(H)** Microscopic observation of *P. gingivalis* mixed with PG-IgY-IR700 before and after NIR irradiation. The asterisk indicates bacterial aggregation induced by the treatment. Arrowheads indicate dispersed bacteria. Scale bar: (refer to scale in image). **(I)** Wound healing (scratch) assay using HPLF cells to evaluate tissue safety. Representative phase-contrast images show cell migration at 0 h and 48 h under Control, NIR-PAT^2 (proposed therapy), and aPDT (antimicrobial photodynamic therapy) conditions. Blue boxes indicate the magnified areas shown in the right column. **(J)** Quantitative analysis of the closed area percentage in the wound healing assay. The NIR-PAT^2 group showed no significant difference (ns) compared to the Control, whereas aPDT significantly inhibited wound closure ($P < 0.05$)

Biosciences (NB, USA). All other chemicals were of reagent grade.

Culture

P. gingivalis (ATCC 33277), *T. forsythia* (JCM 10827), and *T. denticola* (JCM 8152) was obtained from EW Nutrition's Japan Immunology Laboratory. *P. gingivalis* is an obligate anaerobe and was incubated at 37°C with a deoxygenation/carbon dioxide generator (Anaero Pack; Mitsubishi Gas Chemical Company, Tokyo, Japan), adjusted to at least 15% carbon dioxide and 0.1% oxygen. Gifu Anaerobic Broth-Modified (GAM) "Nissui" or GAM agar "Nissui" (Nissui Pharmaceutical Co., Ltd., Tokyo, Japan) was used as the bacterial culture medium. All *P. gingivalis* used in the experiments were on a logarithmic growth curve and were adjusted and used at 1.0×10^5–1.0×10^7 cells/mL.

T. forsythia, and *T. denticola* were anaerobically cultured in modified GAM broth supplemented with normal rabbit serum (20 mL/L), thiamine (10 μg/mL), and NAM (10 μg/mL).

Synthesis of IR700-conjugated IgY

IgY against *P. gingivalis* was obtained from the Immunology Laboratory of EW Nutrition Japan, Inc. IgY against *P. gingivalis* was prepared by immunosensitizing 18-week-old Hy-Line hens with *P. gingivalis* and infecting them twice; yolks were collected from eggs produced between 2 and 6 weeks after the second infection and powdered. The IgY antibody was partially purified from the powdered yolk by chloroform extraction and ammonium sulfate precipitation. The partially purified lyophilized IgY was further purified using the Pierce Thiophilic Adsorption Kit (Thermo Fisher Scientific, Waltham, MA, USA) (Fig. 1A).

IgY was incubated with IR700 and 0.1 mol/L Na_2HPO_4 (pH 8.6) for an hour at 15–25 °C under shielded light. The conjugate of IgY and IR700 was designated PG-IgY-IR700. The conjugate was purified using a Sephadex G50 column (PD-10; GE Healthcare, NJ, USA). Protein concentrations were determined by measuring the absorbance at 595 nm using a spectrophotometer (UV1900i; Shimadzu, Kyoto, Japan) and the Coomassie Plus Protein Assay Kit (Thermo Fischer Scientific) [33]. The concentration of IR700 was determined based on absorbance at 689 nm through spectrophotometry and on the number of fluorescent molecules bound to IgY. The binding ratio of IR700 was adjusted such that two to three molecules of IR700 bound to one molecule of IgY. SDS-PAGE analysis of each conjugate was performed according to a previously published method. Diluted IgY without the IR700 conjugate was used as a control, and the fluorescent bands were measured in the 689 nm fluorescence channel using Pearl Trilogy (LI-COR Biosciences).

Cell culture

HPLF were purchased from ScienCell Research Laboratories, Inc. (Carlsbad, CA, USA) and cultured in Dulbecco's Modified Eagle's medium (Fujifilm Wako Pure Chemicals, Osaka, Japan) containing 100 U/mL penicillin and 100 μg/mL streptomycin (Penicillin-Streptomycin Solution (×100); Fujifilm Wako Pure Chemicals, Osaka, Japan) and 10% fetal bovine serum at 37 °C under 5% carbon dioxide and 95% air.

In vitro NIR-PAT^2

P. gingivalis (1.0×10^5 cells/mL) was seeded in 1.5 mL microtubule. The medium was replaced with phosphate-buffered saline (PBS), and PG-IgY-IR700 was added at a final concentration of 200 μg/mL, resulting in a total volume of 1 mL. The cells were subjected to light-shielded anaerobic incubation at 37 °C for 1 h and irradiated with a laser (MLL-III-690 nm laser, CNI Laser, Changchun, China) at 256 J/cm^2 [34]. The NIR wavelength and irradiation dose were referred to as NIR-PAT^2 for C. albicans [35]. The *P. gingivalis* colonies were incubated at 15 ~25°C for 3 h after irradiation and counted on a modified GAM agar medium. The PI non-staining rate was measured through flow cytometry (Gallios; Beckman Coulter, CA, USA).

Evaluation of NIR-PAT^2 cytotoxicity

The effects of NIR-PAT^2 and aPDT on cells were examined through a wound-healing assay. The 24-well plates were seeded with HPLF and cultured to 80% confluency; approximately 1.0-mm-wide scratches were added. HPLF (5.0×10^5 cells) were treated with aPDT and NIR-PAT^2. aPDT was adjusted with TBO at a final concentration of 0.33 mM and irradiated with a red LED (L690-66-60; Usio-Epitex, Kyoto, Japan) at 60 mW/cm^2 for 5 min [36]. After 48 h, the degree of containment of the scratch area was evaluated using Image J software.

Flow cytometry

To evaluate the binding of PG-IgY-IR700 to *P. gingivalis* and HPLF, IgY-I700 at 200 μg/mL was mixed and incubated for 1 h. The fluorescence of *P. gingivalis* and HPLF at 700 nm was measured through flow cytometry (Gallios; Beckman Coulter, CA, USA) and analyzed using the Kaluza software (Beckman Coulter).

To investigate the bactericidal effect of NIR-PAT^2 on *P. gingivalis*, PI fluorescence was measured through flow cytometry after staining with PI (final concentration, 1 μg/mL; Thermo Fisher Scientific). *P. gingivalis* was treated with NIR-PAT^2, incubated for 4 h, and stained with PI for 30 min. PI-positive bacteria were detected by flow cytometry, and the viability of *P. gingivalis* was analyzed based on the PI-negative rate.

Measurement of CFUs

P. gingivalis cells treated with NIR-PAT^2 were diluted 10^3- to 10^4-fold in PBS and cultured on GAM agar medium. The number of *P. gingivalis* colonies was measured after their formation.

Fluorescence microscopy

To confirm the bactericidal effect of NIR-PAT^2, *P. gingivalis* and PG-IgY-IR700 were incubated at 37 °C for 3 h and washed with PBS. *P. gingivalis* was treated with 70% ethanol for 15 min and washed with PBS 1.0×10^5. *P. gingivalis* was seeded into 3.5-mm glass bottom dishes coated with poly-D-lysine. PI (final concentration, 1 μg/mL; Thermo Fisher Scientific) was added 30 min before observation.

Scanning electron microscopy

Electron microscopy was used to detect the changes in the surface structure. *P. gingivalis* was harvested at 15–25 °C 3 h after NIR-PAT^2 treatment and washed with PBS. *P. gingivalis* was fixed in 2% glutaraldehyde (TAAB Laboratories Equipment, Berks, UK) for 24 h at 4 °C, washed with PBS for 15 min, and fixed again in 2% osmium (VIII) oxide solution (Fujifilm Wako Pure Chemicals, Osaka, Japan) at 4 °C for 2 h. The specimens were subjected to dehydration using graded ethanol concentrations (50, 60, 70, 80, 90, 95, and 99%; 5 min each). *P. gingivalis* was replaced with t-butyl alcohol and lyophilized (VFD-21 S; Vacuum Device; Ibaraki, Japan). The cells were coated with osmium plasma (NL-OPC80NS; Nippon Laser, Tokyo, Japan) and observed under a scanning electron microscope (JSN-7610 F; JEOL, Tokyo, Japan).

Evaluation of LPS levels

The destruction of gram-negative bacteria generates endotoxin. The levels of endotoxin released in the no-treatment, NIR-PAT^2, and aPDT groups were evaluated using the ToxinSensorTM Chromogenic LAL Endotoxin Assay Kit (GenScript). Each sample was spun down, and the treatments were replaced with PBS in the no-treatment group, PG-IgY-IR700 in the NIR-PAT^2 group, and 0.33 mM TBO in the aPDT group as the antimicrobial agents. The endotoxin levels were evaluated 4 h after treatment.

Establishment of a periodontitis mouse model

A periodontitis mouse model was prepared with 8-week-old C57BL/6J female mice purchased from CLEA Japan, Inc. Three mice were housed per cage, with a 12-h light/dark cycle. Periodontitis was induced through silk ligature (Fig. S1A), and *P. gingivalis* infection [37]. During treatment, the mice were anesthetized with isoflurane or intraperitoneal injections of medetomidine hydrochloride (0.3 mg/kg), midazolam (4 mg/kg), and butorphanol tartrate (5 mg/kg). A 5 – 0 silk ligature was placed around the maxillary second molar of each mouse. *P. gingivalis* (1.0×10^9 *P. gingivalis*) was mixed with 50 μL of 2% carboxymethylcellulose (Sigma-Aldrich, St. Louis, MO, USA) and infiltrated into a cotton ball, which was placed in the mouth of the mice until it spontaneously expelled. Cotton balls were infiltrated with PG-IgY-IR700 (200 μg/mL) and placed in the mouth until the mice spontaneously expelled them. Near-infrared irradiation was performed 3 h after antibody administration. In the aPDT group, a cotton ball soaked in 0.33 mM TBO was placed in the oral cavity and held until the mouse spontaneously expelled it (about 2–3 min). In this study, the aPDT parameters were set at a power density of 60 mW/cm^2 for 5 min, resulting in a total energy fluence of 18 J/cm^2. This protocol was selected as it aligns with clinically optimized standards for periodontal photodynamic therapy, which typically range from 10 to 60 J/cm^2. For the Antibiotics group, Amoxicillin was administered via drinking water at a concentration of 500 μg/mL. Based on the average daily water intake for mice (approx. 150 mL/kg body weight), this corresponds to an estimated daily dosage of approximately 75 mg/kg/day.

In vivo NIR-PAT^2 for the periodontitis model

The effect of NIR-PAT^2 in the periodontitis models was evaluated in the four groups and compared. The periodontitis (+) group underwent silk thread ligation of maxillary molars and *P. gingivalis* infection, and the NIR-PAT^2 group underwent PG-IgY-IR700 and NIR irradiation for periodontitis (+). The Sham group underwent only silk thread ligation of the maxillary molars without *P. gingivalis* infection. Each treatment was performed 1 week after the first *P. gingivalis* infection. The mice were irradiated with a 670–710 nm laser (MLL-III-690 nm Laser, CNI Laser) at 0.68 W/cm^2 and 256 J/cm^2 (Fig. S1B). Preoperative and postoperative micro-CT (Latheta LCT-200; Hitachi, Tokyo, Japan) was performed weekly to determine the extent of alveolar bone resorption. The alveolar bone resorption was measured by summing the distance between the cementoenamel junction and alveolar crest at four points on the mesial, distal, buccal, and palatal sides of the right maxillary second molar. Each treatment was administered twice, and the mice were sacrificed a week later.

Evaluation of bone resorption by H&E staining

The maxilla of the sacrificed mice was removed and fixed in 4% paraformaldehyde for 24 h at 15～25°C. After fixation, the specimens were decalcified in 10% EDTA (pH 8.0) for 4 weeks, dehydrated in graded ethanol, washed in xylene, and embedded in paraffin. The specimens were then sectioned sagittally into 5 μm-thick tissue sections and stained with H&E. Histological analysis was performed using an optical microscope.

Randomization and blinding

Mice were randomly allocated to experimental groups using a computerized random number generator to minimize selection bias. To ensure the objectivity of the evaluation and eliminate potential observer bias, all outcome assessments were conducted in a blinded manner. Specifically, for alveolar bone loss measurement and histological scoring, all samples were assigned unique random identification codes by a researcher who was not involved in the evaluation process. The investigators performing the analysis (e.g., bone level measurements and microbiota taxonomy) remained blinded to the treatment allocation until all data analysis was completed. The key to the codes was only unmasked after the statistical results were finalized.

Sample size rationale

We employed a tiered experimental design to strictly adhere to the 3Rs principle (Replacement, Reduction, Refinement).

1. For the primary phenotypic outcome (Alveolar bone resorption): A sample size of $n = 5$ was determined based on preliminary data and power calculations ($\beta > 0.80$ at $\alpha = 0.05$) to sufficiently capture biological variability and ensure robust statistical detection of the therapeutic effect.
2. For the mechanistic microbiome analysis: We selected a representative subset ($n = 3$) from each group. Since Next-Generation Sequencing (NGS) generates high-dimensional data and our preliminary analysis indicated a very large effect size (Hedges' $g > 2.0$) for the treatment, increasing the sample size further would not yield additional biological insight but would violate the ethical principle of Reduction. Therefore, we prioritized ethical considerations by limiting the number of animals for this specific assay while ensuring rigorous evaluation using effect size metrics and 95% confidence intervals.

16S rRNA gene sequencing and bioinformatics

Saliva samples were collected from mice, and 16 S rRNA gene amplicon sequencing was performed by Genome Read Co. (Placeholder for Takamatsu City, Japan). Bacterial DNA was extracted using the Maxwell® RSC Fecal Microbiome DNA Kit (Promega, Madison, WI, USA) according to the manufacturer's instructions. The V3–V4 hypervariable regions of the 16S rRNA gene were amplified, followed by library preparation with index sequences. All samples were processed in a single batch to minimize potential batch effects.

Raw sequencing data were processed using the QIIME 2 platform (version 2023.2) [38]. Demultiplexing and quality filtering were performed using the q2-demux plugin, followed by denoising with DADA2 (via q2-dada2) to generate Amplicon Sequence Variants (ASVs) [39]. All ASVs were aligned using MAFFT (via q2-alignment) and used to construct a phylogeny with FastTree 2 (via q2-phylogeny) [40]. Taxonomic classification was assigned to ASVs using the q2-feature-classifier (naïve Bayes classifier) trained on the SILVA release 138.1 SSU database with a confidence threshold of 99% [41].

Diversity metrics were calculated using q2-diversity after rarefying samples to the minimum sequencing depth. Alpha-diversity was assessed using Shannon's diversity index and Faith's Phylogenetic Diversity (Faith's PD). Beta-diversity was evaluated based on Weighted UniFrac distances, selected to account for both phylogenetic relationships and relative abundances.

To predict the functional potential of the microbiome, PICRUSt2 (Phylogenetic Investigation of Communities by Reconstruction of Unobserved States 2) was employed based on the ASV profiles. Predicted metabolic pathways were annotated according to the MetaCyc database.

Identification of biomarkers

To identify differentially abundant taxa, two complementary approaches were employed:

1. LEfSe (Linear Discriminant Analysis Effect Size): Biomarkers characterizing each group were identified using the Kruskal-Wallis test ($p < 0.05$), followed by Linear Discriminant Analysis (LDA) to estimate effect size. An LDA score > 2.0 was considered significant.
2. ANCOM (Analysis of Composition of Microbiomes): To account for the compositional nature of microbiome data, ANCOM was performed at the genus level. Significant taxa were identified based on the W-statistic.

Statistical analysis and effect size calculation

All statistical analyses and graph generation were performed using GraphPad Prism version 10 (GraphPad Software, Boston, MA, USA) and the QIIME 2 platform (version 2023.2). Data are presented as individual dots representing biological replicates ($n = 3$ per group) or as mean ± standard deviation (SD), unless otherwise specified. A P-value of < 0.05 was considered statistically significant.

Analysis of in vitro and in vivo physiological data

For continuous variables derived from in vitro assays (colony counts, PI staining ratio, wound closure area, and endotoxin concentration) and in vivo alveolar bone resorption measurements, data distributions were assumed to be normal based on the continuous nature of these biological variables, as formal normality tests (e.g., Shapiro-Wilk) lack sufficient statistical power for small sample sizes ($n = 3$). Consequently, comparisons among three or more groups were performed using one-way analysis of variance (ANOVA) followed by Tukey's multiple comparisons test for all-pairwise comparisons. Bacterial colony counts were log-transformed ($\log_{10}$ CFU/mL) prior to statistical analysis to meet the assumption of homoscedasticity.

Global differences in alpha-diversity and functional pathways were evaluated using the Kruskal-Wallis test. Differences in beta-diversity community structure were assessed using PERMANOVA (Permutational Multivariate Analysis of Variance) with 9,999 permutations.

Given the exploratory nature of this study and the ethical constraints on animal usage (adhering to the 3Rs principle), the sample size was limited to $n = 3$ per group. To strictly evaluate the robustness of the therapeutic effects despite the limited sample size, we focused on the magnitude of the effect (Effect Size) rather than relying solely on P-values for pairwise comparisons. Hedges' g (unbiased Cohen's d corrected for small sample sizes) was calculated for key comparisons. Effect sizes were interpreted as: $0.2 \leqq g < 0.5$ (small), $0.5 \leqq g < 0.8$ (medium), and g >0.8 (large). Additionally, the mean difference and its 95% confidence interval (CI) were reported to assess the precision of the estimates. A P-value of < 0.05 was considered statistically significant for global comparisons.

Results

Synthesis of IR700-conjugated IgY

To generate anti-*P. gingivalis* IgY, hens were immunized with P. gingivalis, and then IgY antibodies were extracted and purified from the buried hen eggs (Fig. 1A). Next, to generate the PG-IgY-IR700 complex, 0.1 mol/L Na_2HPO_4, IR700, and IgY were mixed and incubated for 1 h, and then purified using a PD-10 column (Fig. 1B). The purified PG-IgY-IR700 was light blue in color (Fig. 1C). To verify the production of IR700 conjugated to PG-IgY, PG-IgY and PG-IgY-IR700 were subjected to SDS-polyacrylamide gel electrophoresis (SDS-PAGE). IR700 was observed using a Pearl Trilogy fluorescence imager (LI-COR Biosciences), as it emits fluorescence at a wavelength of 700 nm (Fig. 1D). Both PG-IgY and PG-IgY-IR700 were detected at approximately 190 kDa using SDS-PAGE, and fluorescence was negative for PG-IgY that was not combined with IR700. Conversely, IR700 was positive for PG-IgY conjugated to IR700. These data confirm the successful conjugation of IR700 to PG-IgY. Subsequently, binding of the prepared PG-IgY-IR700 was evaluated (Fig. 1D). Fluorescence was observed at 700 nm in the PG-IgY-IR700 solution before NIR-light exposure (Fig. 1E). In contrast, NIR fluorescence in the PG-IgY-IR700 solution was lost upon exposure to NIR-light at a dose of 256 J/cm^2 (Fig. 1E). These results suggest that PG-IgY-IR700 underwent a photochemical reaction that led to aggregation, as previously described (Fig. 1F).

One hour after combining PG-IgY-IR700 with *P. gingivalis* or human periodontal ligament fibroblasts (HPLF), we evaluated the fluorescence of IR700 at 700 nm using flow cytometry (Fig. 1G). *P. gingivalis* mixed with PG-IgY-IR00 exhibited fluorescence at 700 nm. PG-IgY-IR700 binding was also observed in *P. gingivalis* that had undergone various treatments (Fig. S2A). Quantitatively, the Mean Fluoresce.ce Intensity (MFI) increased from 822 (control) to 291,832 (Pg-IgY-IR700), indicating a robust binding affinity. In contrast, no IR700-fluorescence was observed in the HPLF samples with PG-IgY-IR700. This indicates that PG-IgY-IR700 binds to *P. gingivalis* but not to HPLF. IR700 loses fluorescence when exposed to NIR-light at around690 nm. We confirmed the disappearance of IR700-fluorescence, which is the result of aggregation caused by photochemical reactions due to NIR light irradiation, and the PG-IgY-IR700 solution was exposed to NIR-light using a 690-nm light-emitting diode (Fig. S2B).

To observe the aggregation of IR700, *P. gingivalis* cells treated with PG-IgY-IR700 were examined under a stereomicroscope before and after NIR-light exposure (Fig. 1H). As indicated by the arrow (▲), exposure to PG-IgY-IR700 caused *P. gingivalis* to form several small aggregates. As indicated by the asterisk (*), exposure to near-infrared light caused large aggregates to form around IR700.

We subsequently evaluated the cytotoxicity of NIR-PAT^2 and aPDT on HPLF. Cell migration was evaluated using wound healing assays in the control (no treatment), NIR-PAT^2 with PG-IgY-IR700, and aPDT groups. Forty-eight hours after gap formation, the cells in the control and NIR-PAT^2 with PG-IgY-IR700 groups migrated to the gap site. The gap closure area was comparable between the control and NIR-PAT^2 with PG-IgY-IR700 groups at 39.8 ± 1.1% and 36.8 ± 0.6% (control vs. NIR-PAT^2: $p = 0.196$; 95% CI: -1.64 to 7.66; Hedges' g = 2.72), respectively, while cell migration was significantly inhibited in the aPDT group at -1.0 ± 1.4% (vs. Control: $p < 0.001$; 95% CI: 36.08 to 45.38; Hedges' g > 20) (Fig. 1, I and J). The cells in the control and NIR-PAT^2 with PG-IgY-IR700 samples maintained similar morphology, whereas those in the aPDT samples exhibited an anomalous morphology (Fig. 1I). These results indicate that aPDT is cytotoxic to HPLF, whereas NIR-PAT^2 with PG-IgY-IR700 demonstrated no significant cytotoxicity against HPLF.

In vitro effects of NIR-PAT^2 targeting P. gingivalis

The bactericidal effect of NIR-PAT^2 was evaluated by treating monocultures of *P. gingivalis*, *Tannerella forsythia* and *Treponema denticola*. Each bacterium was stained with propidium iodide (PI), a dead-cell stain, and observed under a fluorescence microscope before and after NIR-PAT^2 treatment with PG-IgY-IR700 (Fig. 2A, B, and C). Before NIR-PAT^2 irradiation, *P. gingivalis* was negative for PI staining; after NIR-PAT^2 irradiation, *P. gingivalis* lost IR700-fluorescence, but was positive for PI staining. This was similar to the bactericidal effect of 70% ethanol, which was used as a positive control (Fig. 2A and Fig. S3A). In *T. forsythia* and *T. denitricola*, no IR700-fluorescence was observed, 70% ethanol was PI positive, and NIR-PAT^2 did not show PI positivity (Fig. 2B and C). In the mixed samples of *P. gingivalis*, *T. forsythia*, and *T. denticola*, only *P. gingivalis* was PI positive after NIR-PAT^2 treatment (Fig. 2D), suggesting that NIR-PAT^2 treatment with PG-IgY-IR700 destroyed specifically *P. gingivalis* in a mixed sample of three species.

The NIR-PAT^2-induced morphological changes in *P. gingivalis* were examined using scanning electron microscopy. The samples were fixed and prepared 1 h after each treatment. The surfaces of the control (no treatment) and PG-IgY-IR700-treated *P. gingivalis* groups exhibited a relatively smooth morphology, with no deformation of the bacterial body at immediately after NIR-light irradiation. In contrast, *P. gingivalis* was fragmented and disintegrated after aPDT treatment, which is a thought to be an apoptosis effect (Fig. S4A). These results indicate that NIR-PAT^2 lead unique anti-bacterial effect with maintaining the form with making pore in the surface of the targeting germ. On the other hand, aPDT lead germ cell death with conventional aPDT mechanism.

In vitro NIR-PAT^2

Since NIR-PAT^2 had an effective bactericidal effect on *P. gingivalis* and altered its morphology, we evaluated its efficiency in the control (no-treatment), NIR irradiation only, PG-IgY-IR700 only, and NIR-PAT^2 treatment groups. The bactericidal efficacy was evaluated based on the number of colony-forming units (CFUs) of viable bacteria using flow cytometry and the bacterial survival rate based on the PI fluorescence negative rate. The number of colonies formed was $4.1 \times 10^4 \pm 8.7 \times 10^3$ cells/mL in the control group, $4.4 \times 10^4 \pm 4.7 \times 10^3$ cells/mL in the NIR irradiation group, $3.6 \times 10^4 \pm 2.3 \times 10^3$ cells/mL in the PG-IgY-IR700 (200 μg/mL) group, $2.2 \times 10^4 \pm 4.0 \times 10^2$ cells/mL in the NIR-PAT^2 (10 μg/mL) group, $1.1 \times 10^4 \pm 4.8 \times 10^2$ cells/mL in the NIR-PAT^2 (100 μg/mL) group, and $4.0 \times 10^3 \pm 5.7 \times 10^2$ cells/mL in the NIR-PAT^2 (200 μg/mL) group (Fig. 3A). The control, NIR irradiation, and PG-IgY-IR700 samples formed similar numbers of colonies. In contrast, the number of colonies formed in the NIR-PAT^2-treated samples was significantly lower than that in the control samples ($p < 0.001$; 95% CI: 13,339 to 61,995; Hedges' g = 2.81). The number of colonies formed after treatment with NIR-PAT^2 (100 μg/mL) and NIR-PAT^2 (200 μg/mL) decreased in a concentration-dependent manner (Fig. 3B). Each sample was PI-stained, and P. gingivalis viability was analyzed and compared based on PI-negative rates using flow cytometry. The PI-negative rates for the NIR irradiation and PG-IgY-IR700 groups were 70.5% ± 3.5% and 84.9% ± 0.9%, respectively, comparable to those of 77.9% ± 2.8% in the control group. In contrast, the NIR-PAT^2-treated samples had a PI-negative rate of 18.8% ± 2.6%, which was significantly lower than that of control samples ($p < 0.001$; 95% CI: 48.48 to 69.66; Hedges' g = 10.12) (Fig. 3, C and D).

Furthermore, we confirmed a strong positive correlation between the PI-non-stained rate and the Log10 CFU counts across the treatment groups (Fig. S5) (Pearson's $r = 0.986$, $p < 0.0001$). This quantitative consistency reinforces that the loss of membrane integrity induced by NIR-PAT^2 directly corresponds to bacterial cell death.

NIR-PAT^2 for periodontitis mouse model

After confirming the bactericidal effect of NIR-PAT^2 on *P. gingivalis* in vitro, we examined its therapeutic effects in a mouse model of periodontitis. Periodontitis model mice

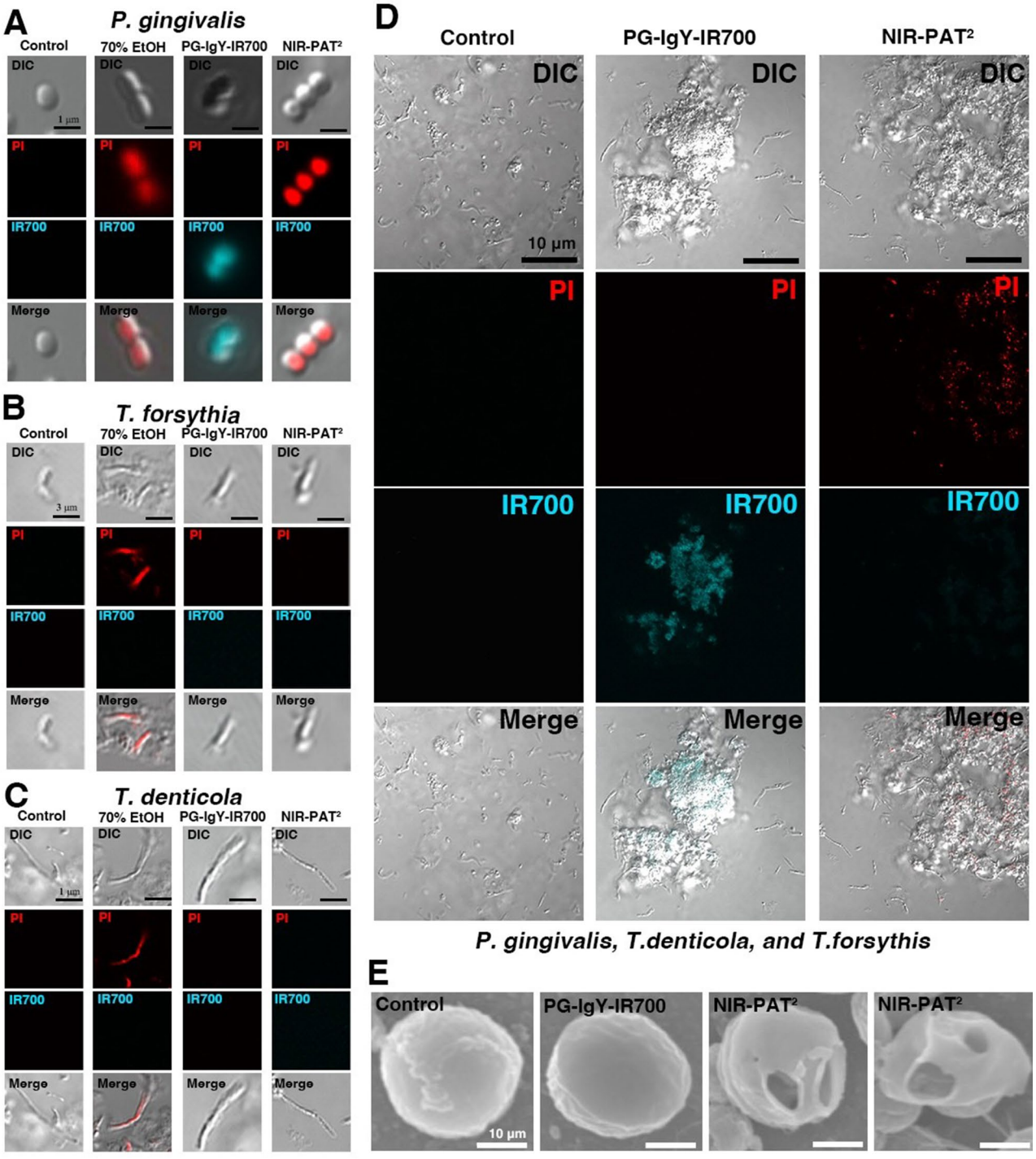

Fig. 2 Bactericidal effect of NIR-PAT^2 on *P. gingivalis*. **(A**, **B**, **and C)** Observation of *P. gingivalis* by fluorescence microscopy. *P. gingivalis*, *T. forsythia*, *and T.denticola* and PG-IgY-IR700 were incubated for 4 h and irradiated with NIR 256 J/cm^2. The bacteria were stained with PI (necrotic cell stain) for 30 min, and the fluorescence of IR700 and PI was observed by fluorescence microscopy. Then, 70% ethanol-treated *P. gingivalis* was prepared as a positive control for PI staining. Scale bar: (A, and C) 1 μm, (B) 3 μm. **(D)** Mixed cultures of *P. gingivalis*, *T. forsythia*, and *T. denticola* were added to PG-IgY-IR700 for 4 h and irradiated with near infrared 256 J/cm^2. The bacteria were stained with PI (necrotic cell stain) for 30 min, and the fluorescence of IR700 and PI was observed under a fluorescence microscope. Scale bar: 10 μm. **(E)** The morphology of *P. gingivalis* was observed through scanning electron microscopy. The morphology of the bacterial surface appeared unchanged in the control (no treatment) samples and those treated with PG-IgY-IR700 alone. The bacteria in the NIR-PAT^2-treated samples appeared deformed and destroyed. Scale bar: 0.5 μm

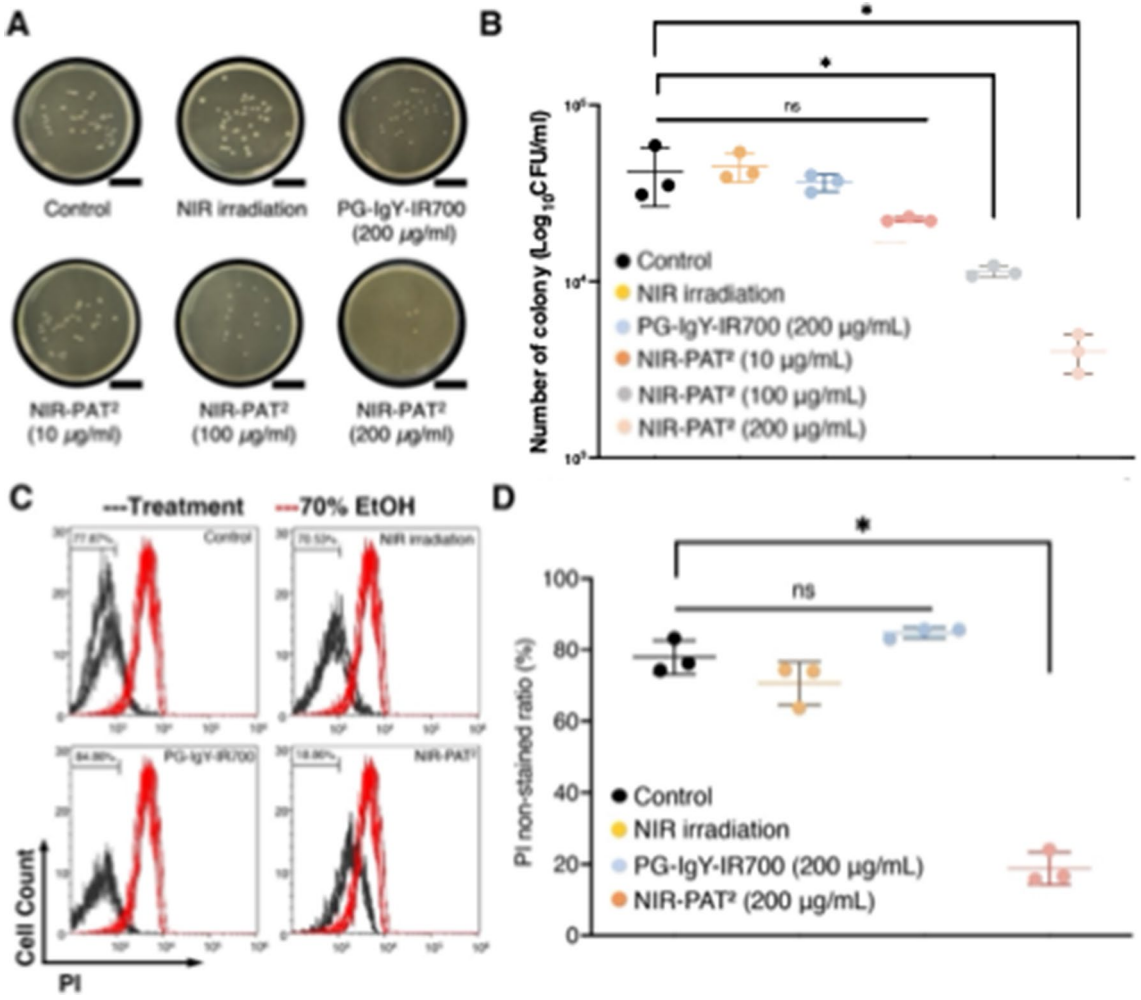

Fig. 3 . Investigation of the bactericidal effects of NIR-PAT^2. **(A, and B)** After each treatment, the samples were cultured on a GAM agar medium, and the number of colonies formed was determined. A: The agar medium for each sample is shown. Scale bar: 3 cm. B: The number of colonies formed is presented and compared with those in the control (no-treated) samples. The effect of NIR-PAT^2 was enhanced by PG-IgY-IR700 in a concentration-dependent manner. Data are presented as mean ± SD. $n = 3$. *P<0.05 compared to control samples. (Detailed statistical parameters, including exact P-values, 95% CIs, and effect sizes, are provided in the main text.). **(C, and D)** Each sample was PI-stained and analyzed for the PI-nonstained ratio by flow cytometry to assess *P. gingivalis* viability. *P. gingivalis* treated with 70% ethanol was used as a positive control for PI staining. Survival rates for NIR irradiation alone and PG-IgY-IR700 alone were similar to those of the control (no-treated) samples; however, those for NIR-PAT^2 were lower. The data are presented as mean ± SD. *P <0.05 compared to control samples. (Detailed statistical parameters, including exact P-values, 95% CIs, and effect sizes, are provided in the main text.). ns; not significant. $n = 3$

were generated and treated according to the schedule shown in Fig. 4A. Alveolar bone resorption in the Sham, periodontitis (+), and NIR-PAT^2 groups up to 7 days after silk ligation and infection were similar: 0.74 ± 0.054 mm, 0.75 ± 0.019 mm, and 0.73 ± 0.050 mm, respectively.

Alveolar bone resorption values at Day 14 in the sham, periodontitis (+), and NIR-PAT^2 groups were 0.77 ± 0.082 mm, 0.93 ± 0.018 mm, and 0.77 ± 0.085 mm, respectively. The NIR-PAT^2 group showed significantly less alveolar bone resorption than the periodontitis (+) group ($p < 0.001$; 95% CI: 0.065 to 0.255; Hedges' g = 2.45), and the extent of alveolar bone resorption was comparable to that of the sham group without *P. gingivalis* infection (Fig. 4B and C).

On Day 21, alveolar bone resorption values in the sham, periodontitis (+), and NIR-PAT^2 groups were 0.80 ± 0.079 mm, 0.98 ± 0.022 mm, and 0.81 ± 0.063 mm, respectively, indicating that alveolar bone destruction in the sham and NIR-PAT^2 groups was lower than that in the periodontitis (+) group (NIR-PAT^2 vs. Periodontitis (+): $p < 0.001$; 95% CI: 0.095 to 0.233; Hedges' g = 3.12). Histological analysis supported these findings, showing reduced alveolar bone destruction in the NIR-PAT^2-treated group (Fig. 4D).

Evaluation of lipopolysaccharide release

The aim of the experiment was to compare the release of lipopolysaccharide (LPS), a potent inflammatory

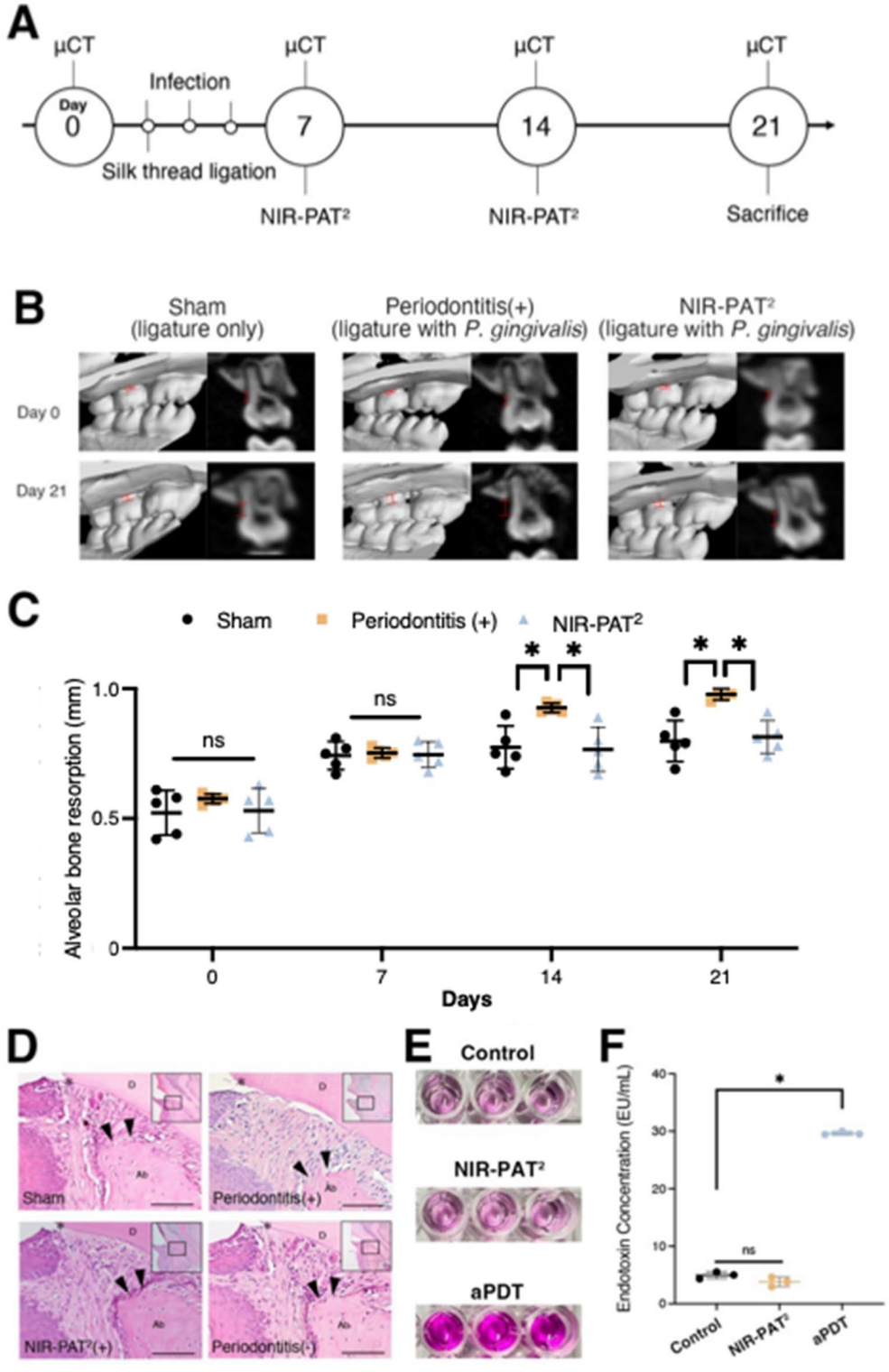

Fig. 4 (See legend on next page.)

molecule, from *P. gingivalis* bacteria after treatment with two different methods: NIR-PAT^2 and aPDT. We evaluated the release of lipopolysaccharide (LPS) from *P. gingivalis* using NIR-PAT^2 cells in vitro. Samples treated with aPDT were prepared and underwent NIR-PAT^2. After each treatment, LPS in the supernatant was evaluated using the ToxinSensorTM Chromogenic LAL Endotoxin Assay Kit (GenScript). First, the LPS in each reagent was

(See figure on previous page.)

Fig. 4 Therapeutic effects of NIR-PAT^2 in a periodontitis mouse model. **(A)** The experimental schedule in vivo is shown. To evaluate the bactericidal effect of NIR-PAT^2, the Sham group underwent only silk ligature placement, and the *P. gingivalis*-infected group underwent both silk ligature placement and *P. gingivalis* infection. Micro-CT was performed every week to evaluate the extent of alveolar bone resorption. **(B)** Micro-CT of the maxillary second molar before and after treatment (left: 3D construction image. Right: coronal plane of the maxillary second molar). **(C)** The extent of alveolar bone resorption around the maxillary second molar was quantified on the micro-CT scans. The total distance between the CEJ and the alveolar defect depth on the proximal, distal, buccal, and palatal sides was measured. The data are presented as mean ± SD.*$P < 0.05$ compared with periodontitis (+). (Detailed statistical parameters are provided in the main text.) $n = 5$. **(D)** Histological evaluation of periodontal tissues. *: CEJ; arrows: alveolar apex; D: Dentin, Ab: alveolar bone. Scale bar: 50 μm. **(E and F)** The amount of LPS released by *P. gingivalis* after each treatment in vitro was compared. The data are presented as mean ± SD. *$P < 0.05$ compared with control (no-treated) samples. (Detailed statistical parameters are provided in the main text.). ns; not significant

quantified and used as a blank for each sample (Fig. S6A and B). Since the amount of released LPS depends on the number of killed bacteria, the treatment parameters for NIR-PAT^2 (PG-IgY-IR700 100 μg/mL) and aPDT (0.33 mM TBO) were adjusted to achieve equivalent bactericidal effects (Fig. S5C). LPS detection levels in the NIR-PAT^2 and aPDT samples were 3.82 EU/mL ± 0.48 EU/mL and 29.64 EU/mL ± 0.17 EU/mL, respectively. NIR-PAT^2 significantly suppressed LPS release compared to aPDT ($p < 0.001$; 95% CI: 25.04 to 26.60; Hedges' g > 20) (Fig. 4, E and F). Furthermore, the LPS level in the NIR-PAT^2 group remained as low as that in the control group (4.97 ± 0.60 μg/mL), with no significant difference observed ($p = 0.125$; 95% CI: -0.49 to 2.79; Hedges' g = 1.27). The results clearly showed that NIR-PAT^2 significantly suppressed LPS release compared to aPDT.

Impact of NIR-PAT^2 on global microbial diversity and community structure

To evaluate the therapeutic potential of NIR-PAT^2 in modulating the oral ecosystem, we initially assessed the α-diversity indices (Fig. 5A–C). Kruskal-Wallis tests revealed highly significant differences among the five experimental groups across all assessed metrics, including Observed features ($p = 0.0001$), Shannon index ($p = 0.013$), and Faith's Phylogenetic Diversity ($p = 0.0003$). Although the limited sample size ($n = 3$ per group) inherent to this exploratory study precluded statistical significance in post-hoc pairwise comparisons, the magnitude of the biological difference was substantial. For instance, comparing the dysbiotic Periodontitis group to the NIR-PAT^2 group, the stabilization of Faith's PD exhibited a large effect size ($p = 0.0003$, Hedges' g = 7.51, 95% CI: 31.67 to 51.83), suggesting a robust prevention of dysbiotic expansion. Similarly, other indices showed remarkably large effect sizes, such as Observed features ($p = 0.0001$, Hedges' g = 8.96,95% CI: 163.49 to 246.51) and Shannon index ($p = 0.013$, Hedges' g = 7.78, 95% CI: 1.41 to 2.27), further corroborating the potent modulatory effect of NIR-PAT^2 on microbial richness and evenness.

This structural shift was further corroborated by β-diversity analysis based on Weighted UniFrac distances (Fig. 5D). PERMANOVA confirmed a robust and statistically significant difference in community composition ($p = 0.001$; $R^2 = 0.865$, Pseudo-F: 16.0787). Notably, the NIR-PAT^2 treated samples clustered near the Health group, indicating a partial restoration toward a healthy-associated profile.

To further assess community stability, we analyzed multivariate dispersion (PERMDISP) (Fig. 5E). The NIR-PAT^2 group maintained low dispersion comparable to the Health group, indicating a stable and reproducible microbial community structure. In stark contrast, the Antibiotics group exhibited significantly higher dispersion, reflecting a destabilized and heterogeneous community state. The increase in dispersion in the Antibiotics group compared to NIR-PAT^2 was substantial ($p < 0.0001$, Mean Difference: 0.125, 95% CI: 0.091 to 0.159), with a remarkably large effect size (Hedges' g = 9.61), underscoring that NIR-PAT^2 modulates the microbiome without inducing the ecological instability often associated with broad-spectrum antimicrobials.

Taxonomic profiling (Fig. 5F) and genus-level heatmap analysis (Fig. 5G) further visualized this shift, showing a consistent suppression of periodontitis-associated taxa across all replicates.

Targeted modulation of key pathogenic and commensal taxa

To comprehensively identify the specific bacterial taxa driving the ecological shifts, we employed Linear discriminant analysis Effect Size (LEfSe) and Analysis of Compositions of Microbiomes (ANCOM) (Fig. 6A, B). LEfSe analysis revealed distinct taxonomic signatures for each group. Notably, the core commensal genus *Streptococcus* was identified as the most robust biomarker characterizing the NIR-PAT^2 group, exhibiting a high LDA score (> 5.0) (Fig. 6A). This suggests that the therapy is uniquely defined by the maintenance of health-associated flora, distinguishing it from the Periodontitis group which was characterized by dysbiotic markers. ANCOM results provided confirmatory evidence, independently identifying *Streptococcus* as a significantly differentially abundant taxon (Fig. 6B).

Building on these profiling results, we next quantified specific microbial biomarkers to elucidate the quality of the microbiome shift (Fig. 6C, D). Kruskal-Wallis tests confirmed significant heterogeneity in the relative abundance of key taxa across the groups. A critical finding

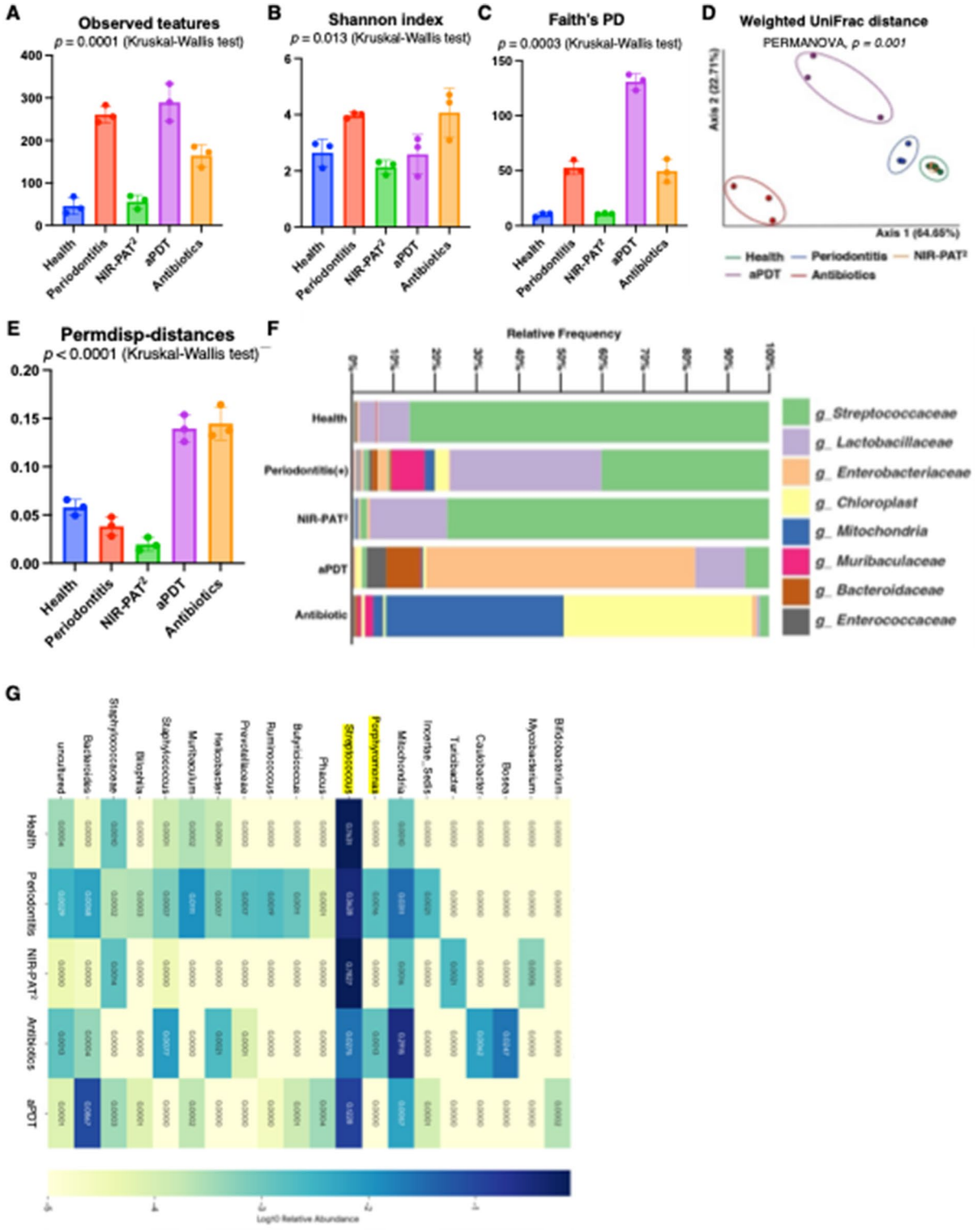

Fig. 5 (See legend on next page.)

was the preservation of the core commensal genus, *Streptococcus* (Fig. 6C). In the NIR-PAT^2 group, the abundance of *Streptococcus* showed no significant difference compared to the Health group (ns). Quantitatively, the difference between NIR-PAT^2 and Health was negligible ($p > 0.999$; ns, Mean Difference: -4.05%, 95% CI: -36.91 to 28.81; Hedges' g = 0.24), confirming that the therapy preserves the integrity of the commensal microbiota.

(See figure on previous page.)

Fig. 5 NIR-PAT^2 treatment drives a compositional shift toward a healthy-associated profile without compromising microbial richness. **(A–C)** α-diversity indices of the oral microbiome: Observed features (A), Shannon index (B), and Faith's PD (C). Data are presented as individual dots representing biological replicates ($n = 3$ per group) with bars indicating the mean ± SD. P-values were calculated using the Kruskal-Wallis test, indicating significant global differences among groups. **(D)** Principal Coordinates Analysis (PCoA) based on Weighted UniFrac distances showing the β-diversity landscape. The overall difference in community structure was confirmed by PERMANOVA ($p = 0.001$). **(E)** Analysis of multivariate dispersion (PERMDISP). The distance to the centroid was calculated to assess community stability. While NIR-PAT^2 maintained low dispersion similar to Health, standard antimicrobials (aPDT and Antibiotics) induced significant community instability (high dispersion). **(F)** Taxonomic composition at the family level, displaying the relative abundance for each individual sample ($n = 15$). **(G)** Heatmap of the top genera visualized on a Log10 relative abundance scale. The NIR-PAT^2 group exhibits a microbial signature distinct from the Periodontitis group and resembling the Health group

This stands in sharp contrast to the dysbiotic Periodontitis group, where Streptococcus was substantially depleted (vs. NIR-PAT^2: $p > 0.999$; ns, Mean Difference: -41.98%, 95% CI: -61.61 to -22.35; Hedges' g = 3.87). Notably, standard antimicrobial treatments failed to maintain this commensal abundance, with *Streptococcus* levels dropping critically in both the aPDT group (Mean: 10.1%) and the Antibiotics group (Mean: 2.5%).

Conversely, the keystone pathogen *Porphyromonas* was significantly suppressed in the NIR-PAT^2 group ($p = 0.016$, Kruskal-Wallis test). The reduction of *Porphyromonas* in the NIR-PAT^2 group compared to the Periodontitis group was biologically profound, demonstrating a very large effect size (Hedges' g = 4.58) and a substantial mean reduction ($p = 0.154$; ns Mean Difference: -0.15, 95% CI: -0.25 to -0.06). Crucially, this pathogen suppression was superior to that of antibiotics. While NIR-PAT^2 reduced *Porphyromonas* to undetectable levels (Mean: 0.00), the Antibiotics group failed to achieve significant reduction (Mean: 0.14), retaining pathogen levels comparable to the Periodontitis group. Furthermore, the abundance of anaerobic bacteria, which characterizes the dysbiotic shift in periodontitis, was drastically reduced by NIR-PAT^2 treatment (Fig. S8). The reduction compared to the Periodontitis group was substantial ($p = 0.0617$; ns, Mean Difference: -15.67%, 95% CI: -22.37 to -8.97), with a very large effect size (Hedges' g = 5.61), demonstrating the potent efficacy of the therapy in eliminating the broad anaerobic pathogen load. These data highlight the selective antimicrobial capability of NIR-PAT^2, which orchestrates a favorable ecological shift by targeting pathogens while sparing commensal residents.

Functional reprogramming of the oral microbiome

To explore whether the observed taxonomic shifts translated into metabolic alterations, we performed predictive functional profiling (Fig. 6E–G). A Kruskal-Wallis test revealed highly significant differences in the global functional landscapes across the groups ($p < 0.0001$). Consistent with the taxonomic restoration, NIR-PAT^2 treatment induced a partial restoration of the functional signature toward a healthy state. Specifically, pathways associated with Lipopolysaccharide (LPS) Biosynthesis—a primary driver of periodontal inflammation—were significantly modulated ($p < 0.0001$, Kruskal-Wallis test). The attenuation of LPS biosynthesis in the NIR-PAT^2 group compared to the Periodontitis group was marked by a high effect size (Hedges' g = 6.22) and a clear confidence interval of the difference ($p > 0.9999$, Mean Difference: -13217, 95% CI: -19164 to -7270) (Fig. 6E). Crucially, this functional restoration was unique to NIR-PAT^2. Standard antimicrobial therapies failed to suppress LPS biosynthesis pathways; in fact, the Antibiotics group exhibited a paradoxical and substantial increase in LPS biosynthetic potential compared to the Periodontitis group ($p > 0.9999$, Mean Difference: +24305, 95% CI: 18698 to 29912; Hedges' g = 9.80). Furthermore, metabolic pathways such as Glucose Metabolism (Fig. 6F) and Mixed Acid Fermentation (Fig. 6G) exhibited similar patterns of recovery. For Glucose Metabolism, the NIR-PAT^2 group showed a marked reduction compared to Periodontitis ($p = 0.2248$, Mean Difference: -63,030, 95% CI: -82,953 to -43,107; Hedges' g = 5.87), restoring levels comparable to the Health group (Mean: 20,041). Similarly, Mixed Acid Fermentation was substantially downregulated in the NIR-PAT^2 group ($p = 0.523$, Mean Difference: -42,787, 95% CI: -48,103 to -37,471; Hedges' g = 15.22), whereas the Antibiotics group failed to mitigate this metabolic upregulation (Mean: 62,403).

A correlation analysis further revealed a significant positive correlation between *Porphyromonas* abundance and LPS biosynthesis capacity (Spearman $r = 0.564$, $p = 0.029$; Fig. S9), supporting the link between pathogen load and functional dysbiosis.

Discussion

In this study, we demonstrated that NIR-PAT^2 appears to preferentially impact key pathogenic taxa while largely preserving commensals. Based on this unique capability, we propose a novel therapeutic paradigm termed Near-Infrared Photo-Bacterialflora Modulation (NIR-PBAM) technology. Unlike conventional antimicrobial therapies, which only disinfect, NIR-PBAM may facilitate a favorable ecological shift toward a healthy state. This optical manipulation of the bacterial flora resulted in modulating oral dysbiosis and NIR-PAT^2 has shown significant potential for treating periodontitis. These data demonstrated that near infrared photo-bacterialflora modulation technology could control periodontitis through selectively ablating *P.gingivalis* in oral disease flora.

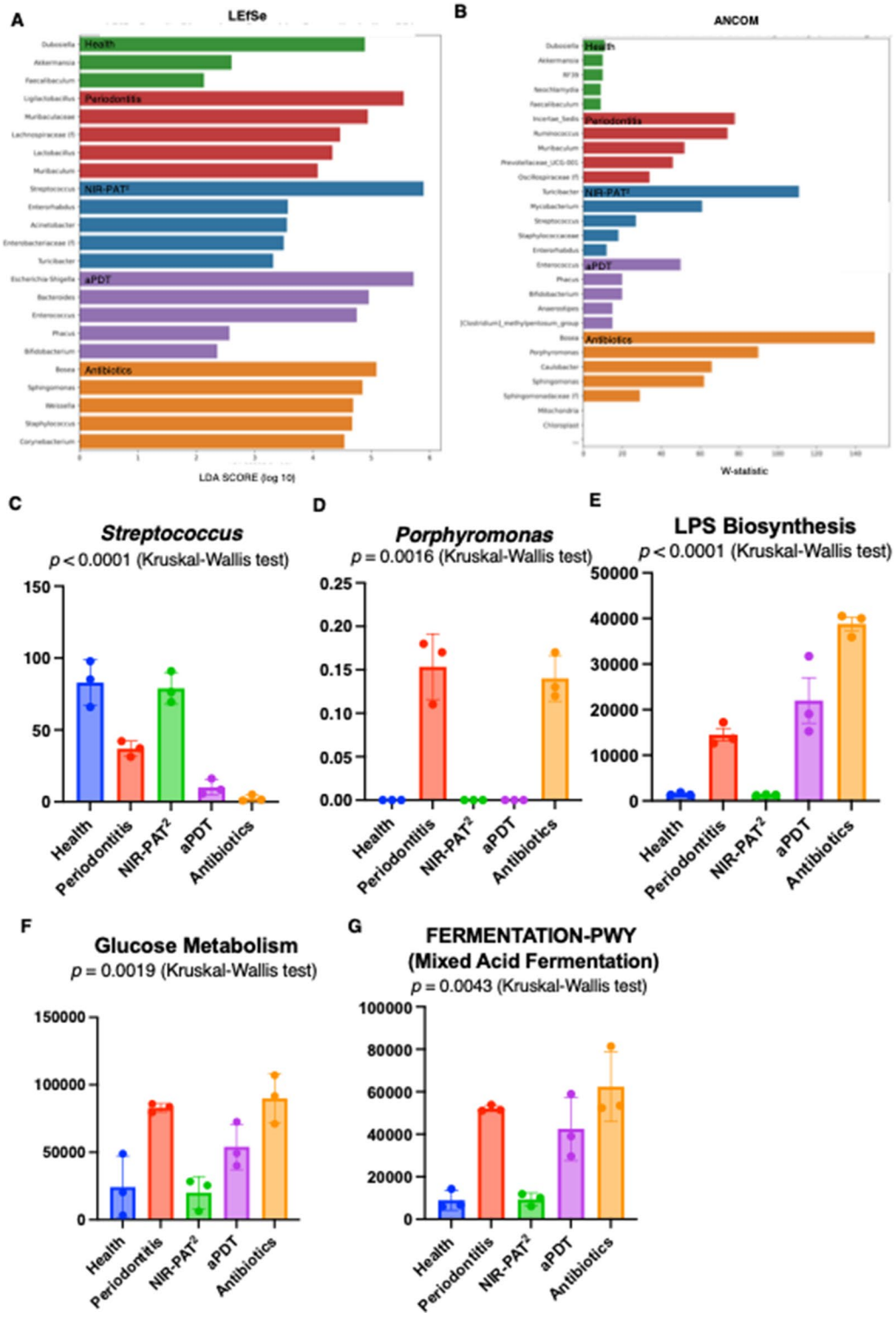

Fig. 6 Selective modulation of key taxa and functional reprogramming by NIR-PAT^2. **(A)** Histogram of Linear Discriminant Analysis (LDA) scores identified by LEfSe, showing biomarkers with differential abundance. **(B)** ANCOM volcano plot highlighting differentially abundant taxa. **(C, D)** Relative abundance of specific genera: the commensal *Streptococcus* (C) and the pathogen *Porphyromonas* (D). *Streptococcus* levels in the NIR-PAT^2 group are preserved (ns vs. Health), whereas *Porphyromonas* is significantly suppressed ($p = 0.016$). **(E–G)** Predicted metabolic pathways using [PICRUSt2/Tax4Fun2]: LPS Biosynthesis (E), Glucose Metabolism (F), and Mixed Acid Fermentation (G). The NIR-PAT^2 treatment demonstrates a consistent trend of reducing inflammatory-associated pathways (LPS Biosynthesis) toward levels observed in the Health group. P-values indicate the global significance determined by the Kruskal-Wallis test

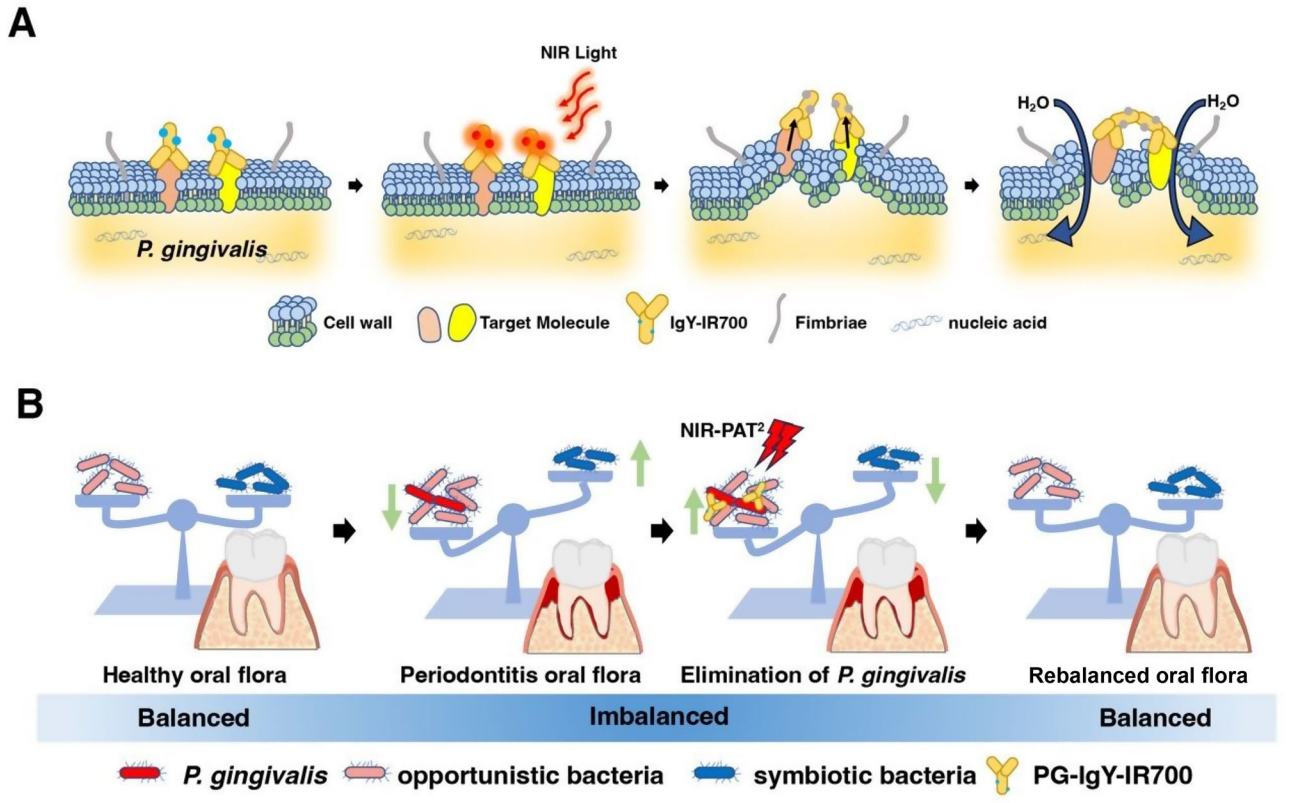

Fig. 7 Schematic diagram of the mechanism of action of NIR-PAT^2. **(A)** PG-IgY-IR700 binds to its target molecule on *P. gingivalis*, and since IgY is a polyclonal antibody, it can target a variety of molecules. When PG-IgY-IR700 bound to *P. gingivalis* is exposed to NIR light, IR700 denatures to a hydrophobic form. At this time, the IR700 expresses fluorescence at around 700 nm wavelength; however, this fluorescence is lost due to hydrophobic denaturation. The loss of hydrophilic side chains causes rapid hydrophobic denaturation of IR700, which then induces hydrophobic aggregation reactions. This aggregation reaction causes physical stress on *P. gingivalis* as the antigen-antibody complex is pulled by IR700. Physical stress deforms the bacterial structure, making it difficult to maintain membrane thickness. This causes the outside water to flow into the bacteria. The bacteria ruptured, causing perforation and deformation. **(B)** Alterations in the homeostasis of the oral microflora. The oral flora affected by Periodontitis is unbalanced, with a disruption of the flora balance. Elimination of *P. gingivalis* by NIR-PAT^2 causes a rebalancing of the oral flora

NIR-PAT^2 enables the selective disinfection of *P. gingivalis*, which causes abnormalities in the oral microflora. Our data revealed that this mechanism is similar to the tumor cell-killing mechanism of NIR-PIT (Fig. 7A) [26]. The mechanism of cell destruction by NIR-PIT is based on a "photochemosis" [42]. The antibody-IR700 complex binds to the cell membrane. Upon irradiation with NIR light, the IR700 ligand (silanol) is released from the antibody-IR700-antigen complex. The release of the silane axis ligand (silanol) causes a change in the hydrophilic/hydrophobic state of IR700, resulting in the aggregation of the antibody-IR700-antigen complex. The process of antibody-IR700-antigen complexation, in conjunction with the physical changes in solubility, leads to the aggregation of the actin cortex, located just below the plasma membrane. This aggregation results in a loss of the cortex's capacity to maintain membrane pressure. Consequently, the cell undergoes an osmotic pressure-induced rupture due to an influx of extracellular water.

This response has been validated under a range of conditions and differs primarily from aPDT in that it is independent of oxidative stress from reactive oxygen species. The elimination of *P. gingivalis* with NIR-PAT^2 did not result in its collapse. Instead, the bacteria exhibited a rupture-like structure with multiple holes, while maintaining their approximate shape. In contrast, aPDT (photodynamic elimination therapy) increased the oxidative stress of *P. gingivalis* due to the production of ROS, resulting in bacterial cell death (Fig. S4A). These results suggest that NIR-PAT^2 may result in lower LPS detection than aPDT. It is possible that NIR-PAT^2 induces localized perforations in the *P. gingivalis* membrane. These perforated areas may then aggregate with IR700 instead of dispersing into the surrounding environment. Beyond the reduction in bacterial load, we hypothesize that the specific photophysical mechanism of NIR-PAT^2 may further limit LPS release. Unlike traditional lytic agents that cause cell burst and massive endotoxin release, NIR-PAT^2 is postulated to induce localized damage to the bacterial cell membrane, potentially leading to the aggregation of membrane components with the IR700-antibody complex. It is theoretically possible that this "fixation-like"

effect prevents the dispersion of LPS into the surrounding environment, resulting in lower detectability compared to lytic therapies like aPDT. However, further biochemical analyses, such as Limulus amebocyte lysate (LAL) assays or electron microscopy, are required to confirm the precise structural state of LPS following NIR-PAT^2 treatment.

Current periodontal models posit that periodontitis is not caused by a single pathogen but is driven by polymicrobial synergy and dysbiosis, where keystone taxa such as *Porphyromonas gingivalis* orchestrate a pathogenic community. Our findings align with this concept, demonstrating that NIR-PAT^2 treatment effectively modulates this dysbiotic network. As shown in Fig. 6, the experimental induction of periodontitis led to a broad shift in microbial composition. Crucially, while NIR-PAT^2 significantly suppressed *P. gingivalis* ($p = 0.013$), the therapeutic impact extended beyond the reduction of this single species. We observed a concomitant compositional shift of the entire flora toward a profile resembling the healthy microbiome (Fig. 7B). This suggests that by targeting key components of the "red complex," NIR-PAT^2 disrupts the synergistic interactions that sustain the dysbiotic state, thereby facilitating a partial restoration of host-compatible homeostasis.

A major challenge in periodontal therapy is achieving pathogen reduction without destroying the beneficial commensal microbiota. In this study, NIR-PAT^2 demonstrated a potential to preferentially impact key taxa, exhibiting a more favorable ecological profile compared to conventional antimicrobials. While broad-spectrum aPDT and antibiotics drastically depleted essential commensals, NIR-PAT^2 maintained the abundance of *Streptococcus* at levels statistically comparable to the Health group (Fig. 6C). *Streptococcus* species are integral to oral health, often antagonizing the colonization of pathobionts through the production of hydrogen peroxide and bacteriocins. By sparing these guardian species while reducing the load of key pathobionts, NIR-PAT^2 appears to shift the ecological balance in favor of health, rather than simply disinfecting the periodontal pocket.

The clinical relevance of these structural changes is further supported by the functional shifts in the microbiome. Predictive profiling (Fig. 6E–G) indicated that the dysbiotic community in the Periodontitis group possessed a heightened potential for LPS Biosynthesis, a major driver of host inflammation. NIR-PAT^2 treatment significantly attenuated this collective virulence factor ($p < 0.0001$), bringing it closer to the baseline observed in healthy mice. The correlation between *P. gingivalis* abundance and LPS biosynthesis (Fig. S9) suggests that the reduction of keystone taxa contributes to dampening the overall inflammatory potential of the community. These results imply that NIR-PAT^2 does not merely reduce bacterial load but actively reprograms the functional capacity of the subgingival microbiome toward a less virulent state.

Our study highlights several therapeutic advantages of NIR-PAT^2 against bacterial infection. First, compared with aPDT, NIR-PAT^2 exerted minimal effects on human cells; PG-IgY-IR700 used in NIR-PAT^2 did not bind to HPLF, and NIR irradiation did not impact cell migration or viability (Fig. 1I and K). NIR 690–700 nm possesses non-ionizing properties and prevents DNA damage and harm to normal cells. The NIR-responsive probe IR700, which has a silicon phthalocyanine backbone, is non-phototoxic and non-biotoxic [22, 26]. In addition, the released IR700 side chains are rapidly excreted in the urine [22, 26]. Conversely, aPDT exerts nonselective toxicity to both bacteria and host cells via ROS, whereas NIR-PAT^2 provides selective antibody-based bactericidal activity, which is critical for oral and intestinal bacterial homeostasis.

Second, the bactericidal action of NIR-PAT^2 may inhibit the release of LPS from *P. gingivalis*, *T. forsythia*, *T. denticola*, *Prevotella intermedia*, *Fusobacterium nucleatum* which are representative bacteria associated with periodontitis [43, 44]. All are Gram-negative bacteria that release LPS, a component of the outer membrane, when the outer membrane is degraded by antimicrobial treatment or metabolism [44]. LPS, also known as an endotoxin, activates various complement pathways, resulting in increased production of immune cells and antibodies [45]. Additionally, when it acts on macrophages and fibroblasts, it stimulates the production of various cytokines inducing immune and inflammatory responses [46]. In periodontitis, inflammation is triggered by periodontopathogenic bacteria, and bacterial LPS causes chronic and exacerbated inflammation. Inhibition of LPS production and bacterial elimination is an ideal treatment for periodontitis. In our experimental data, suppression of LPS production was greater with NIR-PAT^2 than with aPDT (Fig. 4E and F). The aPDT fragments and bacterial disintegration (Fig. S3A), whereas NIR-PAT^2 causes multiple perforations in the bacteria without destroying their morphology (Fig. 2E). Aggregate formation was suggested to inhibit LPS release (Fig. 1H).

Third, NIR-PAT^2 may be useful in the treatment of periodontitis because NIR-PAT^2 and aPDT exert their bactericidal effects through a combination of photosensitive substances and light, making light transmission important. NIR penetrates more effectively than visible light and is easily absorbed by fat and water, including blood, at wavelengths greater than 950 nm. Therefore, ranging from 650 to 950 nm wavelengths were considered optimal [30]. The wavelength of light used in NIR-PAT^2 is 690 nm, which falls within this range. With NIR-PAT^2, antibodies migrate to target molecules, even

within complex periodontal tissues. In contrast, aPDT exerts its bactericidal effect through the production of ROS but requires osmotic adjustment of periodontal pockets filled with tissue fluid. In addition, the lifetime of ROS is short, limiting their effect [20, 36].

Fifth, NIR-PAT^2 offers distinct translational advantages over conventional systemic antibiotics. In this study, we utilized Amoxicillin-supplemented drinking water (500 μg/mL) as a standard-of-care control. This concentration corresponds to a daily dosage of approximately 75 mg/kg/day, which is well within the therapeutic range reported to maintain sufficient %T > MIC (time above minimum inhibitory concentration) for significant bactericidal activity in murine models [47]. While systemic Amoxicillin provides sustained exposure mimicking clinical steady-state levels, it inherently lacks the ability to distinguish between pathogens and commensal flora. In contrast, NIR-PBAM technology achieved comparable or superior clinical healing of periodontitis by selectively ablating *P. gingivalis* without the broad-spectrum disruption of the oral microbiome associated with long-term antibiotic use."

Fifth, IgY has several advantages. First, it is less expensive to produce than other antibodies; chickens can produce more than 22.5 g of IgY per year, which is approximately 10% of the target-specific antibody. This is equivalent to the number of IgG antibodies produced by 4.3 rabbits per year [48]. IgY antibodies can also be obtained from chicken eggs without harming the hens. Reportedly, dried IgY preparations do not significantly lose antibody activity after 5–10 years of storage at 4 °C and retain activity for 6 months at 15～25°C and 1 month at 37 °C [49]. For widespread clinical application, it is essential for antibodies to have a long shelf-life. Furthermore, IgY is resistant to proteases. *P. gingivalis*, the subject of this study, is unable to ferment sugars, secrete proteases on the surface and outside the bacteria, utilize proteins and peptides, including immunoglobulins, as energy sources, and evade humoral immune responses against *P. gingivalis* itself [35]. Approximately 80% of the proteases produced and secreted by *P. gingivalis* are trypsin-like [50]. The suppression of immunoglobulin activity of proteases inhibits the immune response. However, IgY is reportedly more resistant to proteolysis than mammalian IgG and retains its activity against trypsin and chymotrypsin [51]. Our data confirm the binding of PG-IgY-IR700 to *P. gingivalis* and demonstrate the bactericidal activity of NIR-PAT^2 (Fig. 2 and S2). IgY is a polyclonal antibody that targets various bacterial antigens. Resistance to antimicrobial therapy requires denaturation and synthesis of target molecules. Synthesis requires multiple genes and resistance to all antigens targeted by IgY is unlikely to coexist [51]. In addition, it is possible that the generated new IgY can accommodate the denatured antigens. Purified IgY does not contain egg albumin and can therefore be used in patients with egg allergy. It also does not bind to protein A/protein G or Fc receptors on mammalian cells. This immune complex does not activate the mammalian complement system or induce inflammation [52].

Limitations of the study

Despite these findings, concerns remain about the clinical application of IgY. First, periodontitis is caused by multiple pathogens and not exclusively by *P. gingivalis.* Although *P. gingivalis* is a keystone pathogen, periodontitis is a polymicrobial disease. Therefore, targeting a single pathogen may not fully address the complex interactions within the entire microbial community. Furthermore, while our analysis demonstrated the preservation of major commensals, the current 16 S rRNA sequencing data cannot fully exclude potential off-target effects on unmeasured or low-abundance taxa within the complex oral biofilm. Therefore, the current findings represent a proof-of-concept for precision targeting, and future comprehensive metagenomic analyses are required to strictly verify the absence of off-target effects. To address these hurdles, the creation of antibody cocktails against multiple periodontitis-causing bacteria could be developed. A single IgY targeting a cross-reactive protein antigen, such as OMP85 in Gram-negative bacteria against multiple bacterial species, would also be useful [53, 54]. The use of common antigens and antibody cocktails may allow a variety of specific bacteria to be eliminated with a single light exposure. Second, the effect of NIR-PAT^2 on target bacteria outside the NIR irradiation zone is unknown. NIR-PIT has been reported to exert an antitumor effect on metastases outside the NIR irradiation zone [22, 30]. Our study confirmed the therapeutic effect on irradiated sites; however, its effect on distant sites was not evaluated. As infections often affect the entire body and are not localized, the potential of NIR-PAT^2 requires further investigation. The development of new delivery methods and devices may complement the potential of NIR-PAT^2 for systemic bacteria such as bacteremia and sepsis.

Third, the efficacy of NIR-PAT^2 is inherently limited by the reach of the antibody and light. Although NIR light (690 nm) penetrates tissue better than visible light does, its intensity decreases in deep periodontal pockets or under thick gingival tissue. This could leave "refuge" areas for *P. gingivalis*. Additionally, delivering the IgY-IR700 probe into the complex architecture of subgingival biofilms is challenging. Future studies should explore advanced delivery systems, such as mucoadhesive hydrogels or nanocarriers, to enhance probe retention and penetration within the biofilm matrix.

Fourth, the method of irradiation must be considered. For example, NIR-PIT and NIR-PAT^2 require exposure

of the target to light rays to induce its effects, and previous studies on NIR-PIT have reported mixed results with external irradiation alone; a combination of external and internal irradiation may provide more effective results. More effective therapeutic results can be obtained by combining external and internal irradiation [55]. In this study, we investigated the therapeutic effects of external irradiation on a single antigen in vivo. However, irradiation within the periodontal pockets, rather than external irradiation alone, may significantly enhance the therapeutic effect. Considering the limited space in periodontal pockets, a suitable light-source device should be developed. Therefore, the development of a light device must be considered [56].

Fifth, although IgY production is more cost-effective and scalable than mammalian IgG, scaling the entire NIR-PAT^2 system for widespread dental practice involves significant logistical considerations. The need for specialized NIR laser equipment and trained operators could hinder its adoption in smaller clinics. Transitioning from experimental settings to large-scale clinical use requires standardizing irradiation protocols and developing portable, affordable light-emitting devices (e.g., intraoral LED trays) to ensure consistent treatment across diverse patient populations. Furthermore, navigating the regulatory pathways for a combination product (biologic IgY + optical device) will require establishing rigorous safety and efficacy standards for both components.

Sixth, we must recognize the limitations of our in vivo model. Our study's relatively short observation period did not allow us to evaluate long-term bone outcomes, such as alveolar bone resorption related to inflammatory markers. Since periodontitis is a chronic disease involving progressive tissue destruction, our model may not accurately reflect its long-term clinical course. Future longitudinal studies are needed to elucidate the correlation between the immediate bactericidal effect of NIR-PAT^2 and the prevention of bone loss and stabilization of chronic inflammation. Additionally, our analysis is limited in its depth of microbiota and functional inferences. Specifically, the predictive functional profiling (e.g., PICRUSt2) provides inferred metabolic potential rather than direct measurement of microbial activity. Therefore, these functional interpretations are strictly predictive and require future validation through metatranscriptomic, proteomic, or metabolomic approaches to confirm the actual metabolic changes following treatment.

Seventh, regarding the in vitro bactericidal evaluation, although we confirmed a strong population-level correlation between membrane integrity (PI staining) and colony formation (CFU), we have not directly verified the non-viability of individual PI-stained bacteria. Future research using single-cell analysis is required to strictly confirm the viability status at the cellular level.

Eighth, the sample size was limited to three biological replicates per group ($n = 3$) for the microbiome analyses. Although this sample size is acceptable in the context of an exploratory preclinical study, our findings, particularly regarding the microbiome analyses, should be interpreted with this limitation in mind. While this design aligns with the ethical principles of animal welfare (the 3Rs) for an exploratory proof-of-concept study, it inherently restricts the statistical power required for rigorous pairwise post-hoc comparisons. Consequently, certain inter-group differences, particularly in α-diversity indices, did not reach statistical significance after correcting for multiple testing.

However, the robustness of our findings is supported by the unmistakable consistency of the data. Despite the small sample size, the global statistical significance was extremely high (Kruskal-Wallis test, $p < 0.001$) across all major metrics. Furthermore, the PCoA analysis demonstrated distinct and non-overlapping clustering for each treatment group, with minimal intra-group variability. This indicates that the therapeutic effect of NIR-PAT^2 is not a result of random chance but represents a strong biological signal with a high effect size.

We also acknowledge that this study focused on a single time point for microbiome analysis. Future investigations should incorporate longitudinal sampling to evaluate the long-term stability of the restored microbiome and to confirm whether the "partially restored" profile is maintained or further improved over time. Nevertheless, the current data provide a compelling and reproducible evidence base that justifies the advancement of NIR-PAT^2 toward larger-scale pre-clinical and clinical trials.

Conclusion

These findings support NIR-PAT^2 as a promising precision antimicrobial approach capable of selectively targeting *P. gingivalis* and modulating disease-associated dysbiosis and suppressing alveolar bone resorption in a murine model. In the future, NIR-PAT^2 could be applied to a variety of other infectious diseases and may be developed as a light-operated bacterial flora modulation technology for clinical use. We named as "NIR-PBAM technology" and this technology may be easy to translate into the dental clinic.

Furthermore, studies employing this technology to eradicate particular bacteria possess the capacity to elucidate the function of each bacterium in the oral and intestinal microbiota. Such investigations have the potential to facilitate a novel comprehension of the relationship between the microbiota and humans by elucidating the correlation between abnormalities in the equilibrium of the gut microbiota and diseases that were previously deemed unrelated.

Abbreviations

NIR-PBM	Near infrared photo-bacterialflora modulation technology
NIR-PAT[2]	Near infrared photo-antibacterial targeting therapy
aPDT	Antimicrobial photodynamic therapy
ROS	Reactive oxygen species
IR700	IRDye700Dx
NIR-PIT	Near-infrared photoimmunotherapy
GAM	Gifu Anaerobic Broth-Modified

Supplementary Information

The online version contains supplementary material available at https://doi.org/10.1186/s12967-026-08336-2.

Supplementary Material 1

Supplementary Material 2

Acknowledgments

We thank Yoshiro Koma (Yamauchi Dental Clinic) and Junna Watanabe (Nagoya University) for their comments and support; Koji Itakura, Ryoko Sakamoto, Ikuyo Mizuguchi, and Eri Yorifuji from the Department of Biomedical Engineering, Nagoya University Graduate School of Medicine, for their technical support and assistance; and the Department of Laboratory Animals and Biomedical Engineering, Nagoya University Graduate School of Medicine, for their support, assistance, and breeding of the mice.

Author contributions

HM contributed to study conception, design, data acquisition, analysis, and interpretation and drafted the manuscript; KSato and KSakai contributed to study conception, design, and data interpretation and drafted and critically revised the manuscript; KS, KS, and RO contributed to data interpretation and critically revised the manuscript; YK, LX, and HY contributed to data acquisition, analysis, and performance and critically revised the manuscript. KU, SR, and VN created and provided IgY against ***P. gingivalis***. HH contributed to the design and critical revision of the manuscript. All authors gave final approval and agreed to accept responsibility for all aspects of this work.

Funding

JSPS KAKENHI grant 19K1919, 21K10067, 18K15923, 21K07217,25K03451, 25K22916. Program for Developing Next-generation Researchers (Japan Science and Technology Agency). Research Grant from The Chemo-Sero-Therapeutic Research Institute. Suzuki-kenzo scholarship. TERUMO Science Foundation. The Hori Science & Arts Foundation. CREST (JPMJCR19H2, JST). FOREST-Souhatsu (JPMJFR2017, JST). AMED Seeds A (26ym0126807j0005, A-226, AMED). GAP-FUND Tongali (JST). Funders provided only financial support and had no role in the study design, data collection, data analysis, interpretation, or writing of the reports.

Data and materials availability

All data needed to evaluate the conclusions in the paper are present in the paper and/or the Supplementary Materials.

Declarations

Study approval

All animal procedures were conducted in accordance with the National Institutes of Health Guidelines for the Care and Use of Laboratory Animals and were approved by the Nagoya University School of Medicine Animal Care and Use Committee (No. 20436, M210473-003, and M220132-002).

Competing interests

The authors declare that they have no competing interests.

Author details

[1]Department of Oral and Maxillofacial Surgery, Nagoya University Hospital, Nagoya, Aichi, Japan
[2]Advanced Analytical and Diagnostic Imaging Center (AADIC) / Medical Engineering Unit (MEU), Nagoya University Institute for Advanced Research, B3 Unit, Nagoya, Aichi, Japan
[3]Nagoya University Institute for Advanced Research, Nagoya, Aichi, Japan
[4]FOREST-Souhatsu, JST, Tokyo, Japan
[5]Department of Oral and Maxillofacial Surgery, Nagoya University Graduate School of Medicine, Nagoya, Aichi, Japan
[6]Immunology Research Institute in Gifu, EW Nutrition Japan, 839-7, Sano, Gifu-city, Gifu 501-1101, Japan
[7]65 Tsurumai-cho, Showa-ku, Nagoya 466-8550, Japan

Received: 7 July 2025 / Accepted: 17 May 2026
Published online: 02 June 2026

References

1. Levy M, Kolodziejczyk AA, Thaiss CA, Elinav E. Dysbiosis and the immune system. Nat Rev Immunol. 2017;17:219–32.
2. Korem T, Zeevi D, Suez J, Weinberger A, Avnit-Sagi T, Pompan-Lotan M, et al. Growth dynamics of gut microbiota in health and disease inferred from single metagenomic samples. Science. 2015;349:1101–6.
3. Cotillard A, Kennedy SP, Kong LC, Prifti E, Pons N, Chatelier EL, et al. Dietary intervention impact on gut microbial gene richness. Nature. 2013;500:585–8.
4. Chow J, Mazmanian SK. A Pathobiont of the Microbiota Balances Host Colonization and Intestinal Inflammation. Cell Host Microbe. 2010;7:265–76.
5. Stecher B, Maier L, Hardt W-D. Blooming in the gut: how dysbiosis might contribute to pathogen evolution. Nat Rev Microbiol. 2013;11:277–84.
6. Hajishengallis G, Liang S, Payne MA, Hashim A, Jotwani R, Eskan MA, et al. Low-Abundance Biofilm Species Orchestrates Inflammatory Periodontal Disease through the Commensal Microbiota and Complement. Cell Host Microbe. 2011;10:497–506.
7. Allen EM, Matthews JB, Halloran DJO, Griffiths HR, Chapple IL. Oxidative and inflammatory status in Type 2 diabetes patients with periodontitis. J Clin Periodontol. 2011;38:894–901.
8. Cheng Z, Meade J, Mankia K, Emery P, Devine DA. Periodontal disease and periodontal bacteria as triggers for rheumatoid arthritis. Best Pr Res Clin Rheumatol. 2017;31:19–30.
9. Amar S, Gokce N, Morgan S, Loukideli M, Dyke TEV, Vita JA. Periodontal Disease Is Associated With Brachial Artery Endothelial Dysfunction and Systemic Inflammation. Arter, Thromb. Vasc Biol. 2003;23:1245–9.
10. Nagasaki A, Sakamoto S, Arai T, Kato M, Ishida E, Furusho H, et al. Elimination of *Porphyromonas gingivalis* inhibits liver fibrosis and inflammation in NASH. J Clin Periodontol. 2021;48:1367–78.
11. Sczepanik FSC, Grossi ML, Casati M, Goldberg M, Glogauer M, Fine N, et al. Periodontitis is an inflammatory disease of oxidative stress: We should treat it that way. Periodontol 2000. 2020;84:45–68.
12. Brennan CA, Garrett WS. Fusobacterium nucleatum — symbiont, opportunist and oncobacterium. Nat Rev Microbiol. 2019;17:156–66.
13. Sanz M, Herrera D, Kebschull M, Chapple I, Jepsen S, Berglundh T, et al. Treatment of stage I–III periodontitis—The EFP S3 level clinical practice guideline. J Clin Periodontol. 2020;47:4–60.
14. Boucher HW, Talbot GH, Bradley JS, Edwards JE, Gilbert D, Rice LB, et al. Bad Bugs, No Drugs: No ESKAPE! An Update from the Infectious Diseases Society of America. Clin Infect Dis. 2009;48:1–12.
15. Carlet J, Pulcini C, Piddock LJV. Antibiotic resistance: a geopolitical issue. Clin Microbiol Infect. 2014;20:949–53.
16. Rams TE, Degener JE, Winkelhoff AJ. Antibiotic Resistance in Human Chronic Periodontitis Microbiota. J Periodontol. 2014;85:160–9.
17. Villafuerte KRV, Martinez CJH, Vieira LHP, Nobre AV. Benefits of Antimicrobial Photodynamic Therapy as an Adjunct to Non-Surgical Periodontal Treatment in Smokers with Periodontitis: A Systematic Review and Meta-Analysis. Medicina. 2023;59:684.
18. Abdellatif HM, Ali D, Divakar DD, BinShabaib MS, ALHarthi SS. Periodontal status and whole salivary adipokines after scaling and root planing with and without adjunct antimicrobial photodynamic therapy in obese patients with periodontitis. Photodiagnosis Photodyn Ther. 2022;40:103112.
19. Baghani Z, Shabestari SB, Karrabi M. Extent of clinical attachment loss as a practical parameter in efficacy of adjunctive photodynamic therapy in stage II - IV grade C Periodontitis (Aggressive periodontitis): A systematic review and meta-analysis. Bosn J Basic Méd Sci. 2022;22:843–61.
20. Cieplik F, Deng D, Crielaard W, Buchalla W, Hellwig E, Al-Ahmad A, et al. Antimicrobial photodynamic therapy – what we know and what we don't. Crit Rev Microbiol. 2018;44:571–89.
21. Salvi GE, Stähli A, Schmidt JC, Ramseier CA, Sculean A, Walter C. Adjunctive laser or antimicrobial photodynamic therapy to non-surgical mechanical

instrumentation in patients with untreated periodontitis: A systematic review and meta-analysis. J Clin Periodontol. 2020;47:176–98.
22. Kobayashi H, Choyke PL. Near-Infrared Photoimmunotherapy of Cancer. Acc Chem Res. 2019;52:2332–9.
23. Yasui H, Nishinaga Y, Taki S, Takahashi K, Isobe Y, Shimizu M, et al. Near-infrared photoimmunotherapy targeting GPR87: Development of a humanised anti-GPR87 mAb and therapeutic efficacy on a lung cancer mouse model. EBioMedicine. 2021;67:103372.
24. Taki S, Matsuoka K, Nishinaga Y, Takahashi K, Yasui H, Koike C, et al. Spatiotemporal depletion of tumor-associated immune checkpoint PD-L1 with near-infrared photoimmunotherapy promotes antitumor immunity. J Immunother Cancer. 2021;9:e003036.
25. Takahashi K, Taki S, Yasui H, Nishinaga Y, Isobe Y, Matsui T, et al. HER2 targeting near-infrared photoimmunotherapy for a CDDP-resistant small-cell lung cancer. Cancer Med. 2021;10:8808–19.
26. Takahashi K, Yasui H, Taki S, Shimizu M, Koike C, Taki K, et al. Near-infrared-induced drug release from antibody–drug double conjugates exerts a cytotoxic photo-bystander effect. Bioeng Transl Med. 2022;7:e10388.
27. Nishinaga Y, Sato K, Yasui H, Taki S, Takahashi K, Shimizu M, et al. Targeted Phototherapy for Malignant Pleural Mesothelioma: Near-Infrared Photoimmunotherapy Targeting Podoplanin. Cells. 2020;9:1019.
28. Isobe Y, Sato K, Nishinaga Y, Takahashi K, Taki S, Yasui H, et al. Near infrared photoimmunotherapy targeting DLL3 for small cell lung cancer. EBioMedicine. 2020;52:102632.
29. Sato K, Sato N, Xu B, Nakamura Y, Nagaya T, Choyke PL, et al. Spatially selective depletion of tumor-associated regulatory T cells with near-infrared photoimmunotherapy. Sci Transl Med. 2016;8:352ra110.
30. Sato K, Ando K, Okuyama S, Moriguchi S, Ogura T, Totoki S, et al. Photoinduced Ligand Release from a Silicon Phthalocyanine Dye Conjugated with Monoclonal Antibodies: A Mechanism of Cancer Cell Cytotoxicity after Near-Infrared Photoimmunotherapy. ACS Cent Sci. 2018;4:1559–69.
31. Yasui H, Takahashi K, Taki S, Shimizu M, Koike C, Umeda K, et al. Near Infrared Photo-Antimicrobial Targeting Therapy for Candida albicans. Adv Ther. 2021;4:2000221.
32. Abusleme L, Hoare A, Hong B, Diaz P. Microbial signatures of health, gingivitis, and periodontitis. Periodontol 2000. 2021;86:57–78.
33. Sato K, Gorka AP, Nagaya T, Michie MS, Nakamura Y, Nani RR, et al. Effect of charge localization on the in vivo optical imaging properties of near-infrared cyanine dye/monoclonal antibody conjugates. Mol Biosyst. 2016;12:3046–56.
34. Ogata F, Nagaya T, Nakamura Y, Sato K, Okuyama S, Maruoka Y, et al. Near-infrared photoimmunotherapy: a comparison of light dosing schedules. Oncotarget. 2017;8:35069–75.
35. Mayrand D, Holt SC. Biology of asaccharolytic black-pigmented Bacteroides species. Microbiol Rev. 1988;52:134–52.
36. Park D, Choi EJ, Weon K-Y, Lee W, Lee SH, Choi J-S, et al. Non-Invasive Photodynamic Therapy against -Periodontitis-causing Bacteria. Sci Rep. 2019;9:8248.
37. Abe T, Hajishengallis G. Optimization of the ligature-induced periodontitis model in mice. J Immunol Methods. 2013;394:49–54.
38. Bolyen E, Rideout JR, Dillon MR, Bokulich NA, Abnet CC, Al-Ghalith GA, et al. Reproducible, interactive, scalable and extensible microbiome data science using QIIME 2. Nat Biotechnol. 2019;37:852–7. https://www.nature.com/articles/s41587-019-0209-9.
39. Callahan BJ, McMurdie PJ, Rosen MJ, Han AW, Johnson AJA, Holmes SP. DADA2: High-resolution sample inference from Illumina amplicon data. Nat Methods. 2016;13:581–3. https://www.nature.com/articles/nmeth.3869.
40. Katoh K, Misawa K, Kuma K, Miyata T. MAFFT: a novel method for rapid multiple sequence alignment based on fast Fourier transform. Nucleic Acids Res. 2002;30:3059–66. https://pmc.ncbi.nlm.nih.gov/articles/PMC135756/.
41. Bokulich NA, Kaehler BD, Rideout JR, Dillon M, Bolyen E, Knight R, et al. Optimizing taxonomic classification of marker-gene amplicon sequences with QIIME 2's q2-feature-classifier plugin. Microbiome. 2018;6:90. https://link.springer.com/article/10.1186/s40168-018-0470-z.
42. Sato K, Okada T, Okada R, Yasui H, Yamada M, Isobe Y et al. Photoinduced actin aggregation involves cell death: a mechanism of cancer cell cytotoxicity after near-infrared photoimmunotherapy. ACS Nano. 2025.
43. Curtis MA, Diaz PI, Dyke TEV. The role of the microbiota in periodontal disease. Periodontol 2000. 2020;83:14–25.
44. Derradjia A, Alanazi H, Park HJ, Djeribi R, Semlali A, Rouabhia M. α-tocopherol decreases interleukin-1β and -6 and increases human β-defensin-1 and -2 secretion in human gingival fibroblasts stimulated with *Porphyromonas gingivalis* lipopolysaccharide. J Periodontal Res. 2016;51:295–303.
45. Poltorak A, Smirnova I, He X, Liu MY, Huffel CV, McNally O, et al. Genetic and physical mapping of the Lps locus: identification of the toll-4 receptor as a candidate gene in the critical region. Blood cells. Mol Dis. 1998;24:340–55.
46. Wu J, Song D, Li Z, Guo B, Xiao Y, Liu W et al. Immunity-and-matrix-regulatory cells derived from human embryonic stem cells safely and effectively treat mouse lung injury and fibrosis. bioRxiv. 2020;2020.04.15.042119.
47. Andes D, Craig WA. Animal model pharmacokinetics and pharmacodynamics: a critical review. Int J Antimicrob Agents. 2002;19:261–8.
48. Xu Y, Jin L, Li X, Zhen Y, Lu Y, Wang L, et al. Application of chicken egg yolk immunoglobulin in land and aquatic animal diseases control. J Biotechnol. 2008;136:S9–10.
49. Carlander D, Kollberg H, Wejåker P-E, Larsson A. Peroral immunotheraphy with yolk antibodies for the prevention and treatment of enteric infections. Immunol Res. 2000;21:1–6.
50. Kadowaki T, Yoneda M, Okamoto K, Maeda K, Yamamoto K. Purification and characterization of a novel arginine-specific cysteine proteinase (argingipain) involved in the pathogenesis of periodontal disease from the culture supernatant of *Porphyromonas gingivalis*. J Biol Chem. 1994;269:21371–8.
51. Rahman S, Nguyen SV Jr., Umeda FCI, Kodama K. Oral passive IgY-based immunotherapeutics. Hum Vaccines Immunother. 2013;9:1039–48.
52. Zhang X, Calvert RA, Sutton BJ, Doré KA. IgY: a key isotype in antibody evolution. Biol Rev. 2017;92:2144–56.
53. Nakao R, Tashiro Y, Nomura N, Kosono S, Ochiai K, Yonezawa H, et al. Glycosylation of the OMP85 homolog of *Porphyromonas gingivalis* and its involvement in biofilm formation. Biochem Biophys Res Commun. 2008;365:784–9. https://pubmed.ncbi.nlm.nih.gov/18029265/.
54. Doyle MT, Bernstein HD. Function of the Omp85 superfamily of outer membrane protein assembly factors and polypeptide transporters. Annu Rev Microbiol. 2022;76:259–79. https://www.annualreviews.org/docserver/fulltext/micro/76/1/annurev-micro-033021-023719.pdf?expires=1779427580&id=id&accname=guest&checksum=B753A6D9A43029E67E31CC2CD89A3DC1.
55. Maruoka Y, Nagaya T, Sato K, Ogata F, Okuyama S, Choyke PL, et al. Near Infrared Photoimmunotherapy with Combined Exposure of External and Interstitial Light Sources. Mol Pharm. 2018;15:3634–41.
56. Tsukamoto T, Fujita Y, Shimogami M, Kaneda K, Seto T, Mizukami K, et al. Inside-the-body light delivery system using endovascular therapy-based light illumination technology. eBioMedicine. 2022;85:104289.

Publisher's note